LINEAR ANALYSIS OF HIPPOCAMPAL LFP: SLOW GAMMA VS HIGH THETA

YUCHEN ZHOU[1], ALEX SHEREMET[1,2], JACK P. KENNEDY[2], AND ANDREW P. MAURER[1,2,3,*]

ABSTRACT. We apply common linear analysis techniques (Fourier and wavelet transforms) to time-series of hippocampal local field potential (LFP) collected from a small population of rats (5 individuals) during awake-behavior in a maze-exploring task, and rest (non-REM sleep). Important characteristics of hippocampal activity, such as the power of the theta rhythm and its harmonics, as well as that of the gamma rhythm, are strongly dependent on the intensity of behavioral activity, as measured by rat speed. A comparison of Fourier and wavelet representation of stationary LFP epochs show that the wavelet representation fails to resolve high-order theta harmonics (24, 32, 40 Hz) that appear well defined in the Fourier analysis and occupy the frequency band of 20-50 Hz, also attributed to the slow gamma rhythm. It seems possible that a misinterpretation of wavelet analysis might be the origin of the identification of the slow gamma rhythm. Such a misidentification would also naturally lead to spurious coupling results between the low gamma and theta oscillations. Theoretically, both transforms can handle arbitrary time-series; however, the Fourier transform is best interpreted for weakly phase-coupled, nearly-Gaussian stochastic processes, while the wavelet transform is most useful when applied to non-stationary, transient processes. Outside their optimal applicability range, both transforms may produce ambiguous, even misleading results. Rather than refuting the existence of slow gamma, our results emphasize the importance of selecting the adequate spectral analysis method for the stochastic process analyzed. To help with the selection, we propose a simple stationarity test based on the integral value of the bicoherence. Further research is needed to separate high order theta harmonics from slow gamma.

Keywords: Hippocampal LFP, Velocity modulation, Wavelet transform, Slow-gamma, Theta harmonics, Stationary, Bispectrum

1 Engineering School of Sustainable Infrastructure and Environment, University of Florida, Gainesville, FL.

2 McKnight Brain Institute, Department of Neuroscience, University of Florida, Gainesville, FL.

3 Department of Biomedical Engineering, University of Florida, Gainesville, FL.

Correspondence*: Andrew P. Maurer, Department of Neuroscience, University of Florida College of Medicine, P.O. Box 100244, 1149 Newell Drive, McKnight Brain Institute, L1-100 Gainesville, FL 32610. drewmaurer@ufl.edu

1. Introduction

The effort of understanding the connection between brain activity and behavior (started as early as [Jung and Kornmüller, 1938, Green and Arduini, 1954, Vanderwolf, 1969, O'keefe and Nadel, 1978, Buzsáki, 2005]) may be described, in essence, as collecting a variety of measurements of brain activity and associating (often statistically) data "features" to classes of behavior. For example, local field potential (LFP) measurements in the hippocampus exhibit well-known, unique, and easily identifiable oscillatory patterns that associate with obvious behavior. The theta rhythm (4-12 Hz) and associated gamma oscillations (approx. 40-100 Hz) [Stumpf, 1965, Buzsáki et al., 1983, Bragin et al., 1995b] are observed during active, awake exploration and REM sleep [Vanderwolf et al., 1975, Vanderwolf, 1969]. More subtle feature such as the phase coupling between theta and gamma are hypothesized to "facilitate" memory encoding and recall [Lisman and Idiart, 1995], with multiple *in vivo* free-behaving studies associating coupling strength to performance in memory dependent tasks. [Bieri et al., 2014, Montgomery et al., 2009, Montgomery and Buzsáki, 2007, Tort et al., 2009, Zheng et al., 2016, 2015]. The sharp-wave/ripple complex (large-amplitude solitary pulse associated with 100-200 Hz oscillations) corresponds to non-REM sleep [Buzsaki, 1986], and is believed to be responsible for the reactivation of memories during off-line periods [Wilson and McNaughton, 1994].

While this associative approach seems simple enough, it is in fact very difficult to implement in practice, due to both the complexity of the system observed (the brain) and difficulty of defining behavior. The brain controls a staggering range of biological functions, in a manner that seems to be at once distributed and tightly integrated. This makes it hard to identify the precise brain region and type of activity "in charge" of a given function (assuming the function is well defined), and, if identified, to select a clear measurement "feature" to associate to behavior. Moreover, defining behavior beyond broad characterizations such as "awake", "active", or "sleep", is itself a challenge, as one can seldom assign clear causal relations to sequences of behavior actions.

As data collection and analysis techniques refine, the need of robust methods becomes more stringent, both for identifying data "features", and behavior markers. A number of recent studies report that rat running-speed is monotonically correlated to the power and frequency of both theta [Whishaw and Vanderwolf, 1973, Morris and Hagan, 1983], and gamma [Chen et al., 2011, Ahmed and Mehta, 2012, Kemere et al., 2013, Zheng et al., 2015] rhythms. This observation is exciting because it suggests an intriguing parametrization of a type of awake-behavior, possibly opening new perspectives for associating brain activity and behavior. It also illustrates the ambiguities of data interpretation and the importance of robust methodologies and data-analysis tools in the identification of finer data "features" associated with behavior. A case in point: using a wavelet transform, Colgin et al. [2009], Belluscio et al. [2012] observed transient bursts frequency range of 20-50 Hz (slow gamma), coupled with the theta rhythm, In the same frequency range, using a different method, Fourier analysis, Scheffer-Teixeira and Tort [2016], Sheremet et al. [2016b,

2018] observed the growth of high-order theta harmonics (24, 32, and 40 Hz; high theta) with increasing rat speed. This begs the question: are "high theta" and "slow gamma" different names for the same process, or are they distinct, coexisting processes? This question might have important behavioral implications, as the frequency band is assumed to play a significant role in spatial navigation [Bieri et al., 2014], attentional selection [Fries et al., 2001] and memory retrieval [Carr et al., 2012, Colgin, 2015].

The answer might be in the analysis techniques used. Here, we explore this possibility by examining both Fourier and wavelet representations of hippocampal local field potential (LFP) traces collected from five rats during two types of behavior: active behavior parameterized by speed, and non-REM rest. The methodology used for classifying behavior and for hippocampal layer identification are presented in section 2. The results of Fourier and wavelet analysis of LFP are presented in section 3, where we also examine the applicability of the two techniques to stochastic processes, make a distinction between stationary and transient processes and propose a simple technique for the stationary/transient classification, based on bispectral analysis. The key findings are summarized in section 4. Details of the mathematics involved, as well as subjects, surgical procedures, and neurophysiology, are included in the appendices.

2. Methods

2.1. **Identification of hippocampal lamination.** Five Fisher344-Brown Norway Rats (r530♂, r538♂, r539♀, r544♀, r695♀) were implanted each with a 32-channel hippocampal probe (appendix A) recording at 24 kHz. To eliminate the effects of anatomic variations between individuals and because the position and orientation of the hippocampal LFP probes cannot be controlled precisely, the position of the hippocampal layers with respect to the recording channels was determined by estimating the distribution of current-source density [e.g., Rappelsberger et al., 1981, Mitzdorf, 1985, Buzsáki et al., 1986, Csicsvari et al., 1999] The current-source density exhibits a unique distribution that is largely independent of anatomic details and that may be used to accurately identify hippocampal layers.

Figure 1 shows the current-source density distribution for theta-dominated awake behavior [Buzsáki et al., 1986, Bragin et al., 1995c, Rappelsberger et al., 1981, Mitzdorf, 1985]. The awake-behavior distribution (figure 1) was estimated using the theta frequency band as well as the first few harmonics (4-30 Hz) of LFP traces corresponding to epochs characterized by rat speed larger than 35 cm/s. The current-source density of theta shows typical phase shift of theta rhythm from oriens to the dentate gyrus [Leung, 1984, Buzsáki et al., 1983, Winson, 1978].

2.2. **Speed as a behavior marker .** Following previous studies [Buzsaki et al., 1983, Terrazas et al., 2005, Maurer et al., 2005, Sheremet et al., 2016a], of particular interest for active behavior is the dependency of LFP characteristics on rat speed. Hippocampal LFP recordings were divided into 1-s segments, which were classified by average speed, thus providing an estimate of the joint

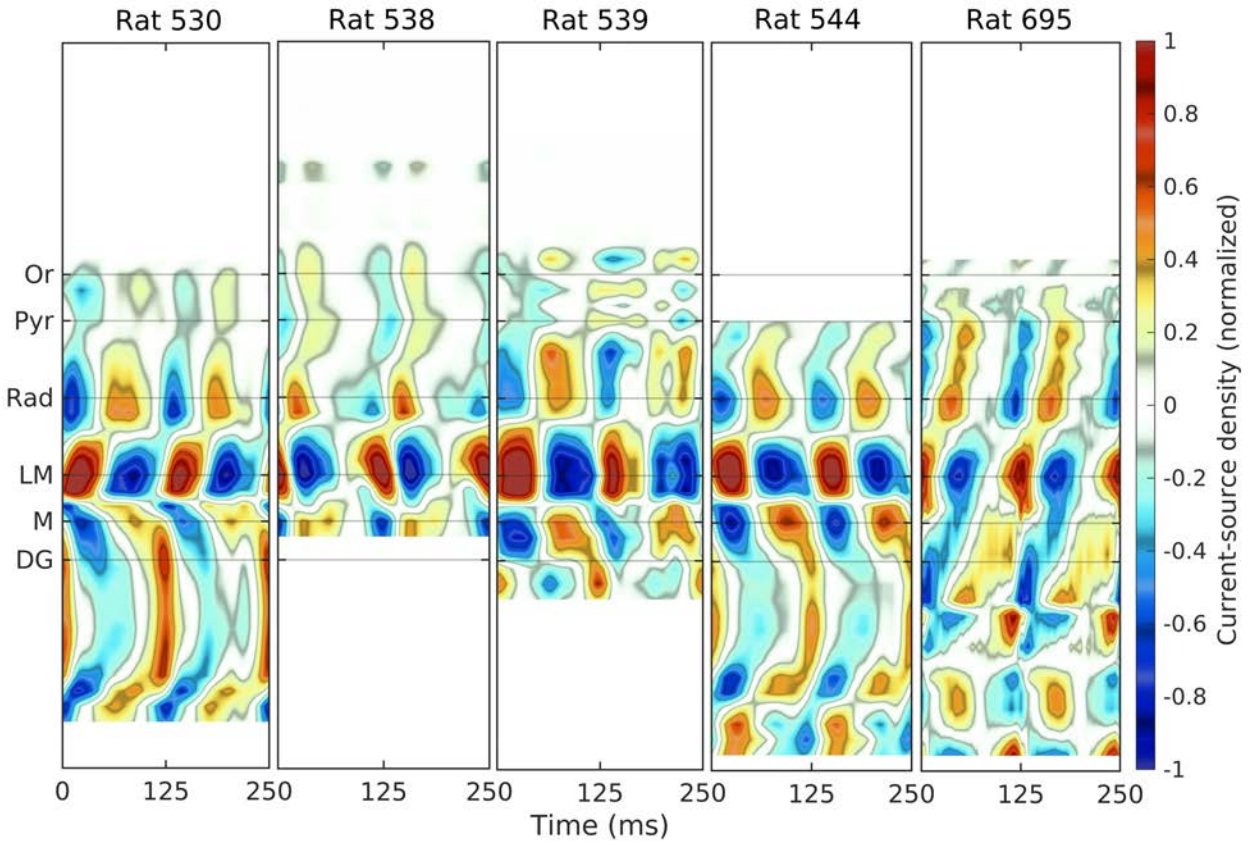

FIGURE 1. Current source density distribution for the examined rats, in awake exploration behavior (LFP theta-dominated LFP traces). In individual rat maps the vertical axis is channel number (not shown). Phase changes across channels (vertical) of the current-source density allow for the identification of oriens (Or), pyramidal layer (Pyr), stratum radiatum (Rad), lacunosum-moleculare (LM), molecular layer (M) and upper granule layer, or dentate gyrus (DG).

probability distribution of rat speed and LFP variance (figure 2). Importantly, variance was chosen over standard post-filtering amplitude method as it is insensitive to a specific frequency range of interest, but took advantage of the power-law shape of the spectra, where lower frequencies (e.g., theta) would carry the majority of the variance. Two speed domains are obvious in figure 2. At low rat speeds (~0-3 cm/s, region A) variance and speed are statistically independent: speed is not a marker for behavior. This region corresponds to low activity, quiescent behavior, or sleep (e.g., REM or non-REM). At speeds larger than, say, 5 cm/s (region B), variance shows a clear correlation to speed. Remarkably, the relation between variance and speed appears to follow the Weber-Fechner law of stimulus perception [Weber, 1860, Fechner, 1860], with LFP variance depending approximately linearly on the logarithm of velocity (red line in figure 2). This suggests that in region B speed may be interpreted and a parameterization of behavior. While the details of this parametrization (range of applicability and coefficients of the linear regression) varies slightly across rats, the monotonic relation provides an important measurable description of behavior.

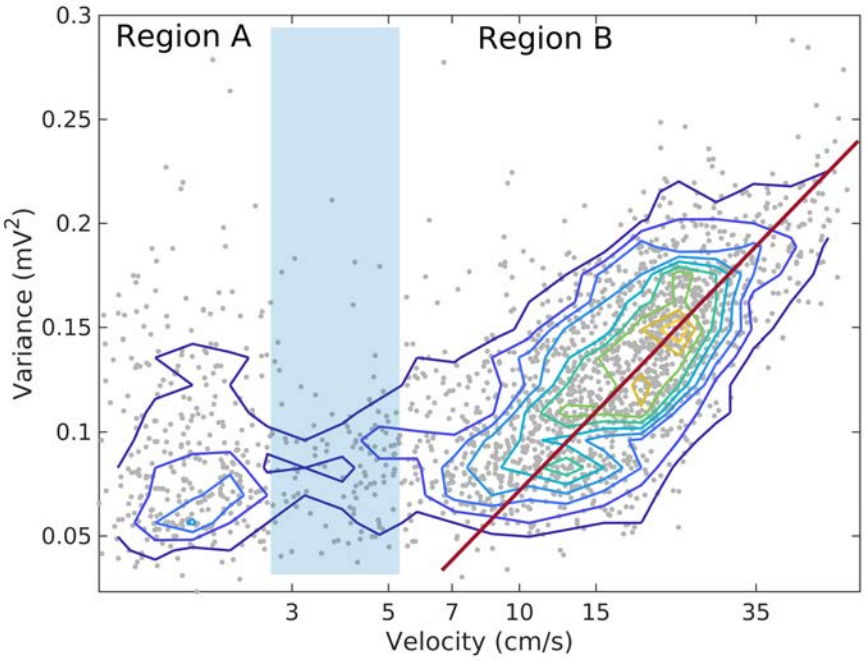

FIGURE 2. Example of joint probability distribution of the variance of hippocampal LFP and velocity (logarithmic scale) for rat r695♀, LM layer. Each gray dot represents one 1-s segment of LFP recording (one realization). Two region may be identified: in region A velocity and variance are approximately statistically independent; in region B, they are correlated. The red line is a linear regression $V = a \log_{10} v + b$, where v is the velocity, V is the variance, and $a = 0.2$, and $b = -0.15$. The transition region (blue) is excluded from this classification.

Below, we use these two regions to classify behavior and discuss results of different analysis techniques. While this classification is obviously crude and broad, with possibly multiple behavior states lumped up into two broad classes (e.g., distinct region-A states may be differentiated using spectral distribution power Grosmark et al., 2012), it is the simplest that suffices for the purpose of this discussion. For region A, we examine non-REM states, that typically exhibit strongly transient LFP signals dominated by sharp-wave/ripple structures [Eschenko et al., 2008, Sullivan et al., 2011, Buzsaki, 2015] in the pyramidal layer, and spikes in the dentate gyrus [Bragin et al., 1995a]. For region B, corresponding to active exploration associated with theta-dominated LFP traces [Green and Arduini, 1954, Vanderwolf, 1969], we examine the dependency on speed of the LFP structure. The transition region (blue shaded area) is difficult to characterize in this simple classification and is not discussed here.

The goal of this study is to investigate the usefulness and limitations of two most common linear analysis techniques, the Fourier and wavelet transform. Therefore, we will not make any assessment about the physiology and structure of the awake-behavior or non-REM sleep. For example, we will not be concerned with evaluating occurrence rates, timing, duration and shape non-REM sharp-wave/ripples complexes [e.g., Wiegand et al., 2016], but will ask instead what is the most adequate data analysis approach for studying them.

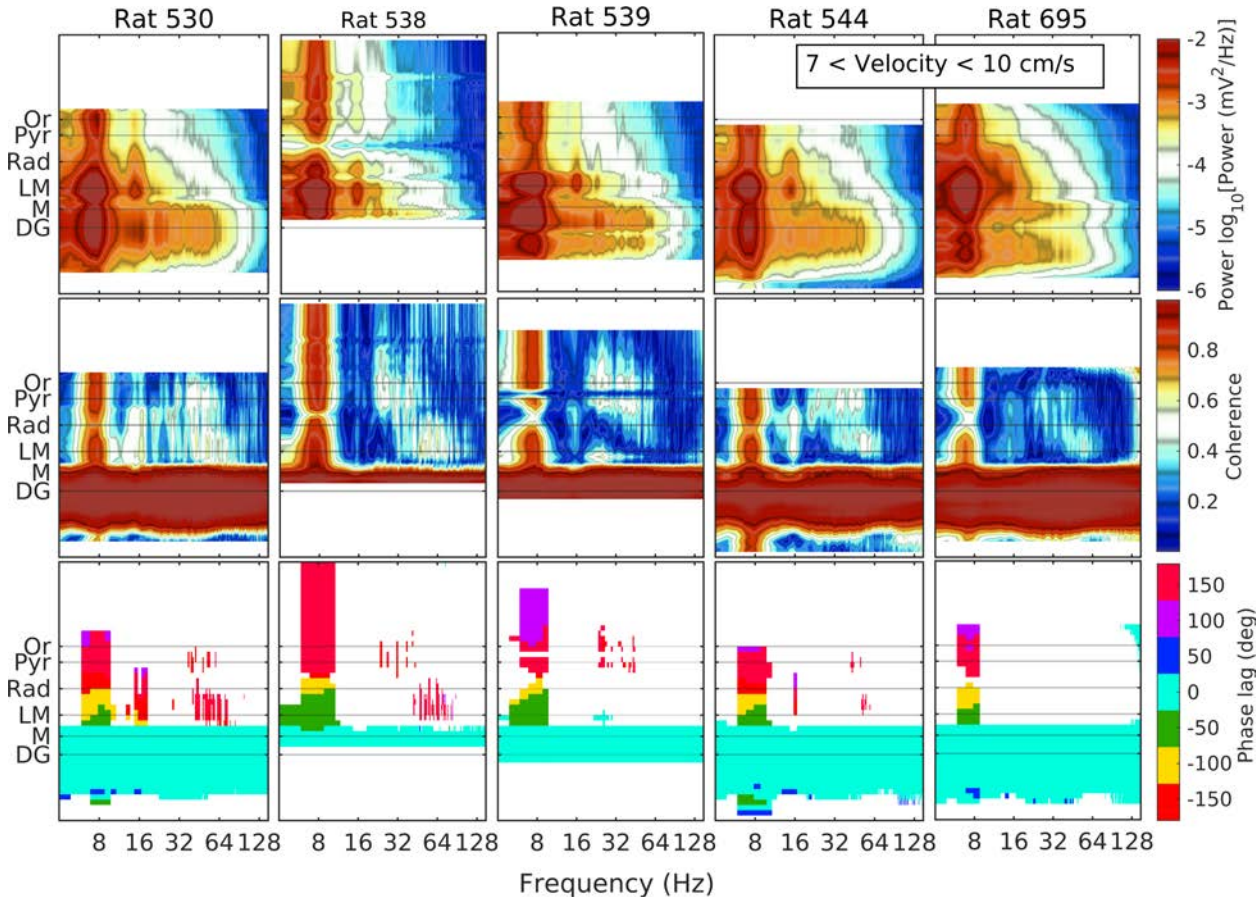

FIGURE 3. Distribution of cross-spectrum over hippocampal layers during active behavior (region B in figure 2), at low speed. Cross-spectra shown are estimated with reference to the DG layer. For each rat, the observed regions of the hippocampus Top: spectral density of LFP variance. Middle: coherence (cross-spectrum modulus). Bottom: phase lag (cross-spectrum argument). On each sub-panel, the vertical axis is channel number (not shown); the panels are aligned according to the layer identification procedure (figure 1).

3. RESULTS

3.1. **Awake behavior (region B).** Previous studies have identified significant changes with running speed in the amplitude and frequency of theta and gamma rhythms [Whishaw and Vanderwolf, 1973, Morris and Hagan, 1983, Kemere et al., 2013, Zheng et al., 2015], as well as the emergence of harmonics of theta, strongly coupled to the theta band [Sheremet et al., 2016b, Scheffer-Teixeira and Tort, 2016]. Here, we revisit these results, with the goal of providing a comprehensive review of observations and their dependence on speed.

3.1.1. *Fourier analysis: theta harmonics.* The Fourier analysis provides a decomposition of the LFP time series into orthogonal harmonic functions uniquely defined by frequency, i.e., number of oscillations per unit of time (see appendix, section B). The average linear structure of the Fourier representation of LFP data collected in different hippocampal layers is fully characterized by the

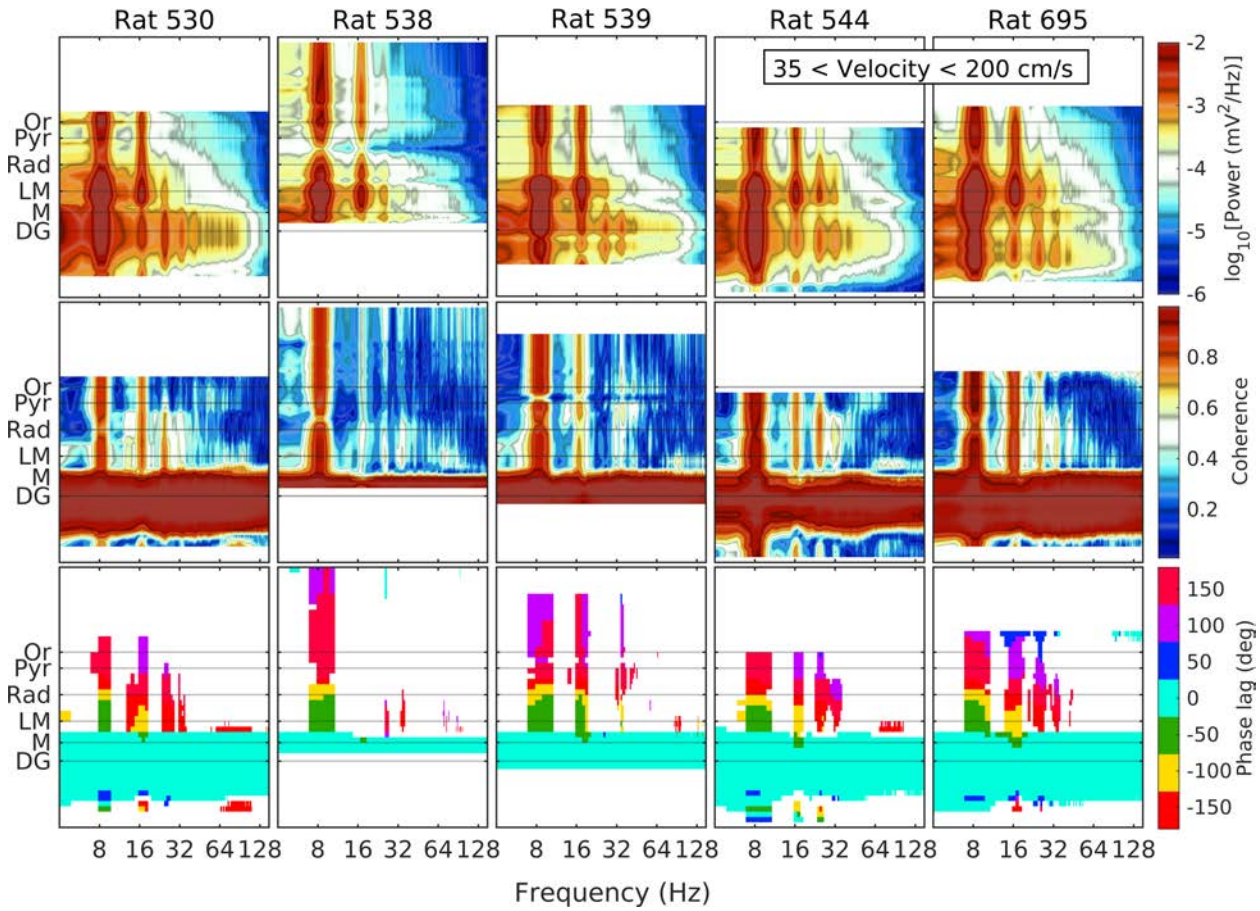

FIGURE 4. Distribution of cross-spectrum over hippocampal layers during active behavior (region B in figure 2), at high speed. Compare with figure 4. Cross-spectra shown are estimated with reference to the DG layer. For each rat, the observed regions of the hippocampus Top: spectral density of LFP variance. Middle: coherence (cross-spectrum modulus). Bottom: phase lag (cross-spectrum argument). On each sub-panel, the vertical axis is channel number (not shown); the panels are aligned according to the layer identification procedure (figure 1).

cross-spectrum matrix (appendix) over spectral densities, coherence, and phase lag (details of the methodology for estimating cross-spectra are given in appendix, section B). The lamina identification map discussed in section 2.1 (figure 1) provides a convenient framework for the examination of LFP power and phase distribution across hippocampal layers and across rat population.

At low speed, the distribution of power across layers is dominated by the LM and DG layers (figure 3). In general, the spectra are rather featureless, exhibiting a broad peak at approximately 8 Hz and,in some cases, extending into lower frequencies (figure 3, rat 539). A weak second harmonic of theta is visible in the LM layer at 16 Hz. The coherence of LM with DG is high throughout the entire frequency range. Across layers (with respect to DG) the coherence is high only in theta band (around 8 Hz; the phase lag is not meaningful unless the coherence is high).

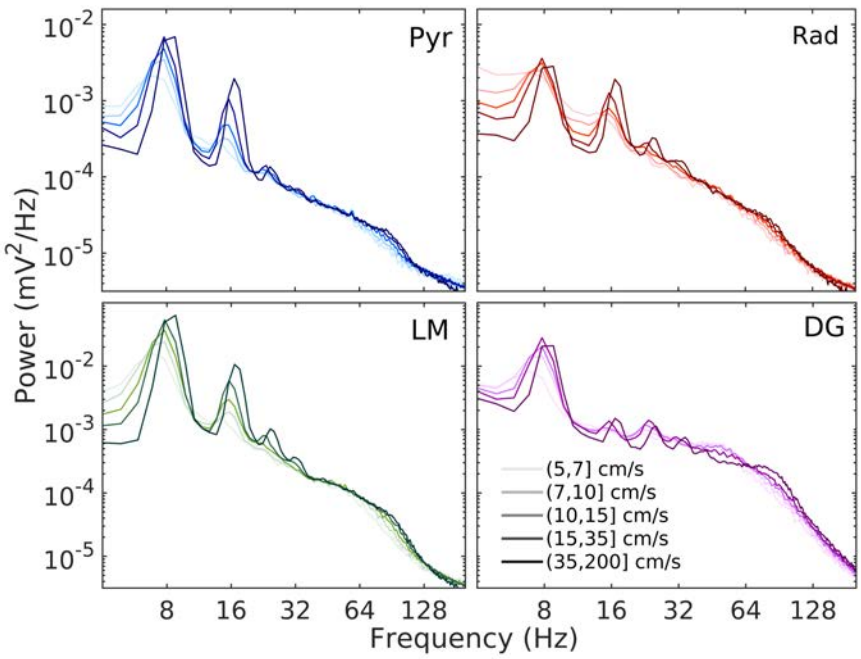

FIGURE 5. Detail of the dependency of spectra density of LFP variance for the Pyr, Rad, LM and DG layers, as function of speed (data collected from rat 539).

At high speeds (figure 4) the theta peak narrows and harmonics of theta appear, highly coherent with theta (figure 4, middle panel). At least four peaks corresponding to frequencies of approximately 16, 24, 32, and 40 Hz are visible in the LM and DG, consistent with previous research [Harper, 1971, Coenen, 1975, Leung et al., 1982, Leung, 1982]. Overall, spectral evolution is remarkably consistent across the examined rat population revealing that the lower frequencies of the hippocampal spectrum are dominated by theta harmonics that develop with velocity. By definition, harmonics have an integer relationship to the fundamental and are phase-coupled. Therefore, unsurprisingly, the phase shift in the harmonics with depth mirror resemble that of the fundamental with the caveat that a substantial amount of the effect is carried by the amplitude/detectability of the harmonic in the decomposition. For example, the pyramidal layer exhibits a low coherence with the DG layer in higher-order harmonics at 24 Hz. It is also worth noting that there is little to no coherence higher frequencies in the dentate gyrus with other lamina of the hippocampus, suggesting that traditional gamma (40-100Hz) can be described as largely "incoherent" across lamina.

A closer examination of the spectra estimates for the Pyr, Rad, LM, and DG layers (figure 5, panel B) allows for some quantification of the evolution of spectral characteristics with speed. All layers exhibit a significant growth of theta amplitude as speed increases, also associated with a narrowing of the theta peak and a slight shift in peak frequency (roughly from 7 Hz to 9 Hz; the resolution of the spectra is 1 Hz; see appendix B). Theta growth also coincides with the growth of additional spectral peaks at harmonic frequencies of theta, most evident in LM and DG spectra, but also, albeit weaker, in the Pyr and Rad layers. In the frequency range occupied by theta and

harmonics (up to ≈ 40 Hz), all spectra shown (figure 5) exhibit a clear power tendency to align to a power law shape $f^{-\alpha}$, but slopes varying with layer. Approximate slopes for the Pyr, Rad and LM are similar ($\alpha_{\text{Pyr}} \approx 1.9$, $\alpha_{\text{Rad}} \approx 2.1$, $\alpha_{\text{LM}} \approx 2.1$); the DG slope stands out as significantly smaller, $\alpha_{\text{DG}} \approx 1.1$. The LFP variance in the gamma range (say, between 40 and 100 Hz) also increases with speed, especially in the LM and DG layers. While the gamma range appears to deviate only slightly from the theta-range slope in the Pyr and Rad layers, and only at large speeds, the LM and DG spectra exhibit significantly steeper gamma slopes.

The Fourier analysis results are consistent with previous studies showing that intense behavior (increased running speed) is associated with an increase in theta power, as well as growth of theta harmonics [Sheremet et al., 2016a]. The higher harmonics observed here occupy the same frequency range as the "slow gamma" observations reported by [Colgin et al., 2009]. The Fourier analysis results, however, do not show any feature that could be construed to represent a new rhythm, with a unique individuality independent of the theta rhythm. However, slow gamma rhythms were identified using not the Fourier but the wavelet representation. Therefore, it behooves us to re-examine the LFP time series presented here using the wavelet representation.

3.1.2. *Wavelet analysis: intermittency.* The wavelet transform decomposes original time series as a superposition of scaled (dilated) and time-shifted "elementary" functions (wavelets, e.g., appendix, section B). For the Morlet wavelets used in this study, the frequency assignment is the center (or spectral peak) frequency (see appendix, subsection B.1.2).

Figure 6 summarizes the wavelet analysis of hippocampal LFP for the Pyr, LM, and DG layers (columns of panels). For any arbitrary time-series segment (figure 6, top row), the wavelet scalogram (figure 6, middle row) shows the frequency distribution of power. Power spectra obtained from wavelet scalograms by reassigning power to frequency instead of scales agree qualitatively with the Fourier spectral estimates (figure 5), but are much smoother (featureless). In particular, the deteriorating frequency resolution at small scales completely removes higher theta harmonics evident in the Fourier spectra (e.g., third harmonic and higher). The situation is more severe in the DG layer, where only the theta peak is discernible.

The examples of scalograms shown in figure 6, middle row, exhibit peaks at theta and its second harmonic as horizontal bands of high power levels, nearly continuous in time (weaker and interrupted perhaps in the DG layer). At higher frequency, however, the power in the frequency bands corresponding to higher theta harmonics (24 Hz, 32 Hz, etc) is not continuous in time (no clear horizontal streaks), but rather has an intermittent-bursting time structure, similar to what originally suggested the existence of the "slow gamma" rhythm.

3.2. **Non-REM sleep.** Recordings of LFP during non-REM sleep are dominated by the sharp-wave/ripple complex [Eschenko et al., 2008, Sullivan et al., 2011, Buzsáki, 2015]. These events appear as transient solitary waves (the sharp wave) synchronous with high frequency oscillations (˜ 200 Hz, ripple).

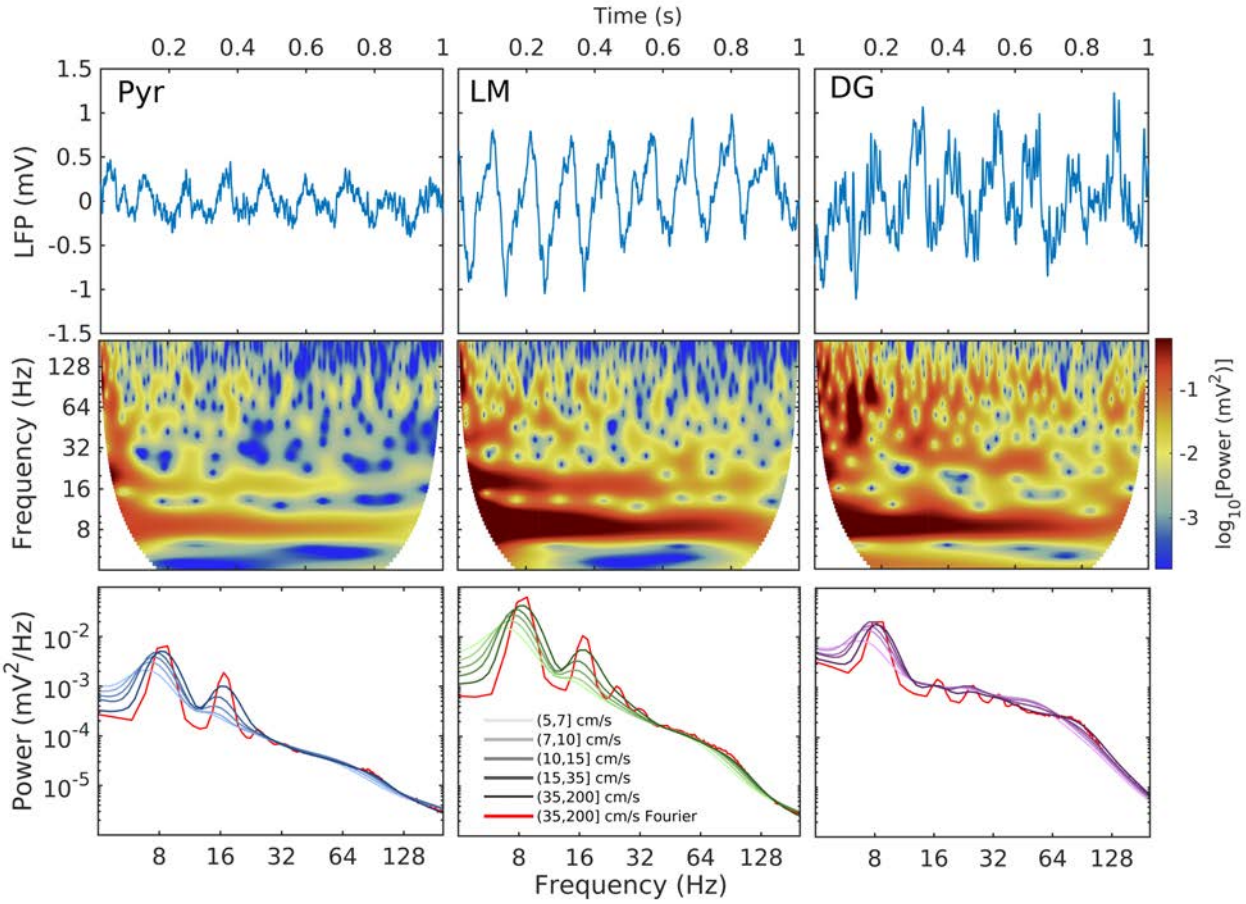

FIGURE 6. Morlet wavelet analysis of hippocampal LFP recorded from rat r530♂during exploration (speed >35 cm/s). Panel columns correspond, from left top right, to LFP recordings in the Pyr, LM, and DG layers. Top row: approximately 8 theta periods of LFP time series. Middle row: corresponding wavelet scalograms in the frequency representation. The true dual space of the wavelet transform is the time-scale two dimensional space. Scales are transformed to frequencies based on central frequency (or peak frequency) of the Morlet wavelet; time intervals near the edges of the scalograms, strongly affected by large edge effects are left blank (white). A sharp oscillation of approximately 0.15-s duration (box in top-right panel) generates a strong multiple-frequency, "intermittent" structure in the scalogram. Because the discrete wavelet transform does not conserve variance [e.g., Daubechies, 1992], wavelet spectra were re-normalized to time-series variance. Fourier spectra (red lines) are given for reference.

Sharp waves change amplitude and polarity depending on the layer. In figure 7, top row, sharp waves vary from positive, ˜1-mV amplitude in the Pyr layer, to negative, ˜ 2 mV amplitude in the Rad layer. In scalograms (wavelet transform; figure 7, middle row), sharp waves can be clearly seen as localized coherent frequency structures resembling triangles of high power concentration. The two sharp-wave-ripple complexes shown in figure 7 cover a frequency range 4 to 150 Hz. In DG, the event synchronous to the sharp-wave/ripples is a 10-ms dentate spike [Bragin et al., 1995a].

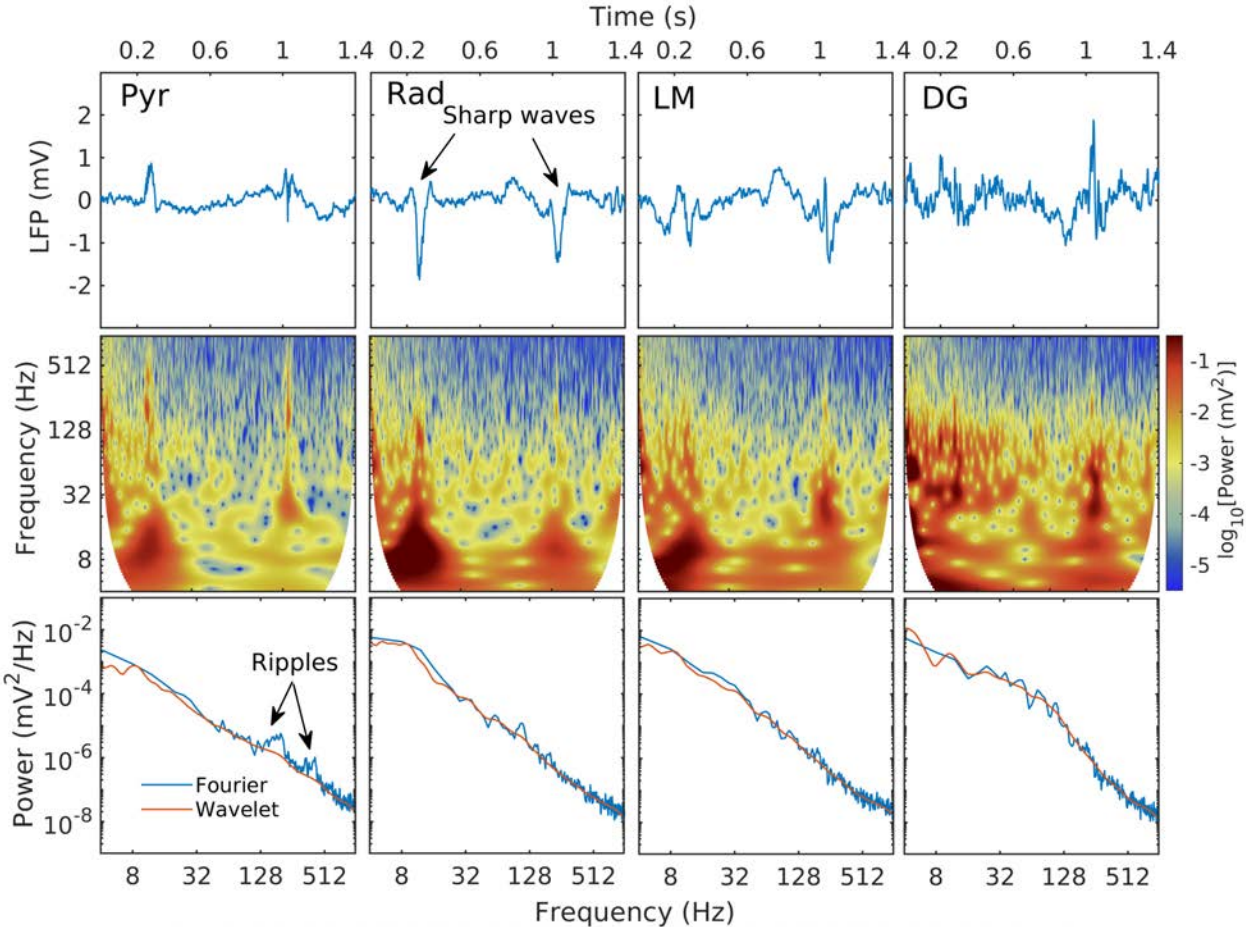

FIGURE 7. An example of analysis of synchronous LFP recordings during non-REM sleep. Panel columns correspond, from left top right, to LFP recordings in the Pyr, Rad, LM, and DG layers. Top row: a time-series segment. Middle row: scalogram. Bottom row: wavelet and Fourier power density spectra estimates.

Estimates of the power spectrum (figure 7, bottom row), computed for both the Fourier and wavelet representation show, as before, rather featureless shapes. The Fourier spectrum of the Pyr-layer signal exhibits two weak peaks that could be related to the ripples of the time series. However, these estimators represent averages over all 1-s time segments of the LFP recordings, while figure 7 shows only one such segment. The time distribution, size, duration, and frequency structure of sharp-wave/ripple events in other segments is certainly different. One is left to wonder what useful information, if any, could be derived from the power spectra for this type of time series.

3.3. **Deterministic series vs stochastic processes.** Without going into details, we will refer here to a given LFP time segment (e.g., top rows of figures 6 or 7) as deterministic. One may try to characterize the features of such time series on their own merit, and discuss, for example, the meaning and details of a particular sharp wave.

The concept of a stochastic process assumes that such time series are in fact random "realizations" of a "virtual" process. When this assumption is made, we expect that each experiment will return a different time series, but as a realization of a unique virtual process, all time series should share some average features that define the individuality of the stochastic process.

3.3.1. *Deterministic time series.* The Fourier and wavelet analysis function on similar principles (appendix, subsection B.1) the signal is analyzed (decomposed) into "elementary" functions. But the similarity ends here.

For the Fourier transform, the "elementary" are harmonic functions uniquely defined by their frequency; they form an orthogonal basis; hence the representation is unique, and has a number of other convenient properties (e.g., conserves variance). The wavelet transform case, the "elementary" functions, the wavelets, form a two-parameter (scale and position on the time axis) set of copies of a fixed shape, the mother wavelet. Wavelets are only required to have near-zero mean and be integrable in some way (fast enough decay at infinity), but are otherwise arbitrary; 2) wavelets do not form (in general) a basis (the representation is in general not unique); and 3) the result is a time-scale representation.

As mathematical, abstract transforms of functions defined on the real axis, both representations work, i.e., they reconstruct the signal exactly (have inverses). In terms of applications to observational data, however, the two transforms were designed to meet different efficiency criteria.

The Fourier transform assumes that the time series is homogeneous in time (stationary). Hence, the main efficiency criterion for the Fourier transform is maximizing ability to interpret the coefficients as amplitudes of harmonic components. This criterion is clearly satisfied for stationary time series, but not for transient signals. The Heisenberg uncertainty relation states that, for a localized signal (inhomogeneous in time, or transient) the number of Fourier components needed to represent the signal is very large. This means that the decomposition is inefficient in practice, but also that the many components needed no longer have the intended meaning; rather, the high frequency components are used only for achieving localization.

The wavelet transform analyzes signals by shifting in time bits of oscillations with different scales (see appendix, subsection B.1.2). This approach is clearly efficient for signals with intermittent bursts of energy. For stationary signals, wavelets are inefficient because they use a two-parameter space when only one is needed (stationarity means some sort of translational invariance in time). The decomposition also loses its intended meaning of identifying intermittent bursts.

Other than paying attention to these elementary efficiencies, the choice of representation (Fourier vs wavelet) for a given time series is arbitrary. There is, however, an elementary fallacy of reasoning that is often encountered: while they are both equally applicable, *the results are not interchangeable*. We stress that the wavelet ordering parameter is *scale* (the value of the dilation parameter) *and not frequenc*y. While scales are often translated to frequencies for ease of interpretation, one should not be confused: Wavelet "frequencies" are, strictly speaking, just labels. Wavelet

have a non-trivial frequency distribution of power, i.e., "comprise" an entire range of (true) Fourier frequencies (appendix, subsection B.1.2). Referring to them as if they had the Fourier meaning is incorrect, and may lead to erroneous conclusions.

3.3.2. *Stochastic processes.* The dissimilarity of the two transforms comes into focus when considering observations as realizations of a stochastic process. In estimating any quantity that is derived by applying an averaging operator, one implicitly assumes that 1) the data are realizations of a stochastic process; 2) that the quantities derived by averaging *exist for that stochastic process*.

In practice, as the stochastic process is a virtual object, not entirely accessible, it is not possible to guarantee the existence of a particular average quantity. Therefore one has to assume a certain model. A rigorous characterization of the properties of the stochastic model, in particular the constraints under which these properties are meaningful, is essential for interpreting statistical estimates of these properties. Otherwise, one runs the risk of elaborating on meaningless, at worst non-existent, entities. This is why the averaged quantities are called "estimators": they are assumed to converge to a well defined value if the averaging is done over the entire realization space.

The choice of the transform should reflect the model we postulate for the stochastic process. This is why the problem of treating the Fourier transform and the wavelet transform as interchangeable is particularly acute for stochastic processes.

For Fourier analysis, a stochastic-process model exists: it is the generalized harmonic process [Priestley, 1981, Percival and Walden, 2009], a zero-mean, variance-stationary process (variance per unit of time is conserved). Without going into the details [e.g., Priestley, 1981, Papoulis and Pillai, 2002, Percival and Walden, 2009, and many others] we state that if the process $x(t)$ is stochastically continuous and stationary, there exists a zero-mean process $X(f)$ with orthogonal increments such that

$$x(t) = \int_{-\infty}^{\infty} e^{2\pi i f t} dX(f). \tag{1}$$

The existence of the spectral density of the process is guarantied by the celebrated Wiener-Khinchin theorem [Priestley, 1981], which states that the power spectral density of process x is the Fourier transform of its auto-covariance function. It is important to note the condition of orthogonality of increments: it means that the Fourier components of different frequencies are *uncorrelated*. Therefore, the Fourier stochastic mode cannot have (does not include) non-stationary realizations such as sharp waves!

As far as we are aware, there no widely-accepted stochastic-process model for transient signals. therefore, it appears that it makes little sense to look for a stochastic scope of the wavelet transform, as it is hard to imagine an overarching stochastic model for non-stationary processes (although recent attempts, e.g., Antoniou and Gustafson, 1999, might still prove this argument wrong). While one is free to average whatever feature seems relevant, we do not in fact know under what conditions a particular average exists.

We illustrate these ideas using synthetic stationary and non-stationary time series.

Figure 8a shows a non-stationary time series composed of solitary sawtooth waves carrying ripples (40 Hz harmonic oscillations windowed to match the peak of the sawtooth wave). The scalogram (figure 8c), shows the typical coherent frequency structure that was also seen in the sharp-wave time series. Generating similar random time series one can construct an average power spectral density (figure 8b). However, we do not know under what conditions this estimator converges, and if so, what it means, therefore we cannot interpret it (it certainly does not mean "variance density").

Figure 8a shows a synthetic stationary time series constructed as a asymmetric ˜ 8 Hz oscillation with a $f^{-1.5}$ background noise, which may be approximated as a generalized harmonic process for which the spectrum exists (figure 8b) and can interpreted as the distribution of variance over Fourier components with different frequencies. The harmonics introduced by skewness appear clearly as peaks in the spectrum. The inadequacy of the wavelet transform as an analysis tool for this type of series is obvious in both the deterministic and stochastic sense. In the stochastic sense: the distortion introduced by the simplistic frequency labeling of wavelets (see appendix, subsection B.1.2) is expressed as a broad smearing of the harmonics (figure 8b). In the deterministic sense: the deterministic scalogram shows obvious intermittent bursts at 32 Hz (4th harmonic), similar to what was called "low gamma" in figure 6. In fact, these features are due to the effect of the fourth harmonic enhancing the asymmetry of the fundamental 8-Hz oscillation (there is no independent 32 Hz oscillation in this time series example!)

3.3.3. *A simple stationarity test.* Based on the above discussion, the Fourier transform seems suitable for time series that can be modeled by a generalized harmonic process. In this case, a host of averaged quantities may be defined to describe second- and higher-order statistics (power spectral density, bispectra, skewness, asymmetry, etc). The wavelet transform seems suitable for transient, non-stationary time series, where averages and estimators such as power spectra should be avoided or used with circumspection.

To distinguish between the two types of time series we propose a test based on the simple idea that a Fourier stochastic process should have at most weakly-correlated frequency components. This implies that the bicoherence of the stochastic process should be weak, therefore the integrated bicoherence (e.g, Elgar 1987, Sheremet et al. 2016b, Kovach et al. 2018; see also appendix, subsection B.2.1) could be used as a test for stationarity.

The bispectra in the examples in figures 9 and 8, panels d, illustrate this property. The stationary series, although weakly asymmetric (not entirely free of cross-spectrum correlation; figure 9c) exhibits a bicoherence that is largely statistically zero, with the exception of the harmonic phase coupling. One could classify this series as matching the generalized harmonic stochastic process. In contrast, the non-stationary example in figure 8 shows large areas of strong coupling, suggesting that this should indeed be classified as non-stationary.

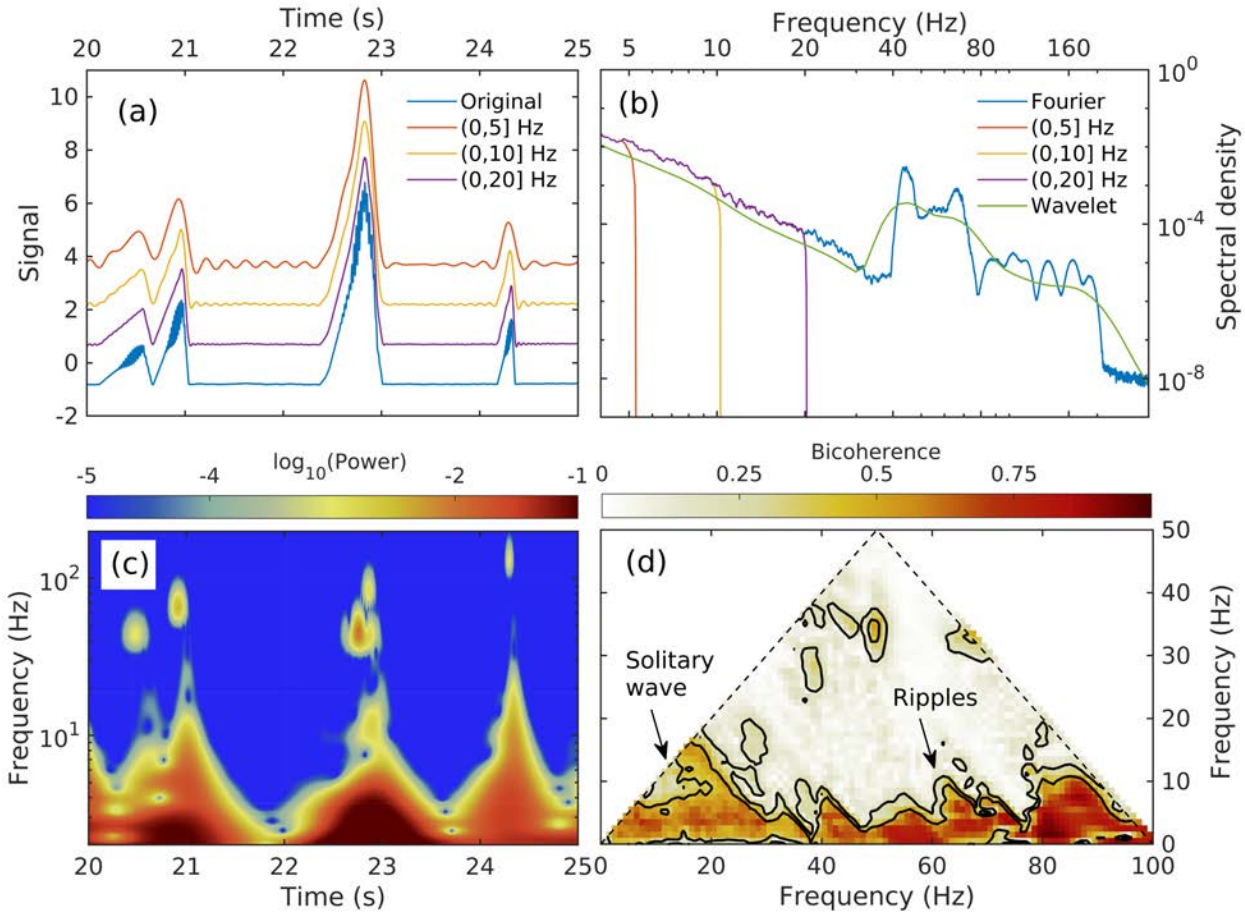

FIGURE 8. Example of Fourier and wavelet analysis of a synthetic time series emulating a sharp-wave/ripples complex. The time series is constructed from a random sequence of solitary saw-tooth pulses carrying synchronous, short trains of high-frequency oscillations (ripples). a) Original time series (blue) and lo-pass filtered time series (see panel b). b) Spectral estimates of the original and filtered time series. The colors correspond to those used in panel a). The power spectral density based on the wavelet transform (green) exhibits a clear low-variance bias. c) Scalogram of the original time series. d) Bicoherence of the original time series. Arrows mark the areas in the bicoherence map corresponding to the phase-coupling between Fourier components that assemble together into the solitary wave, and those that correspond to the coupling between the solitary wave and the ripple trains (see also discussion in text).

The bicoherence map for the LFP observations discussed in section 3, (e.g., figures 6 and 7) are shown in figure 10. The bicoherence maps are similar with the synthetic examples. The integrated bicoherence for the awake -behavior is $\phi \approx 5$, while the value for the non-REM sleep case is $\phi \approx 10$.

4. SUMMARY AND CONCLUSIONS

The present study aims to clarify the usefulness and limitations of Fourier and wavelet transform in the analysis of hippocampal LFP recordings. The Fourier transform has been widely adopted as

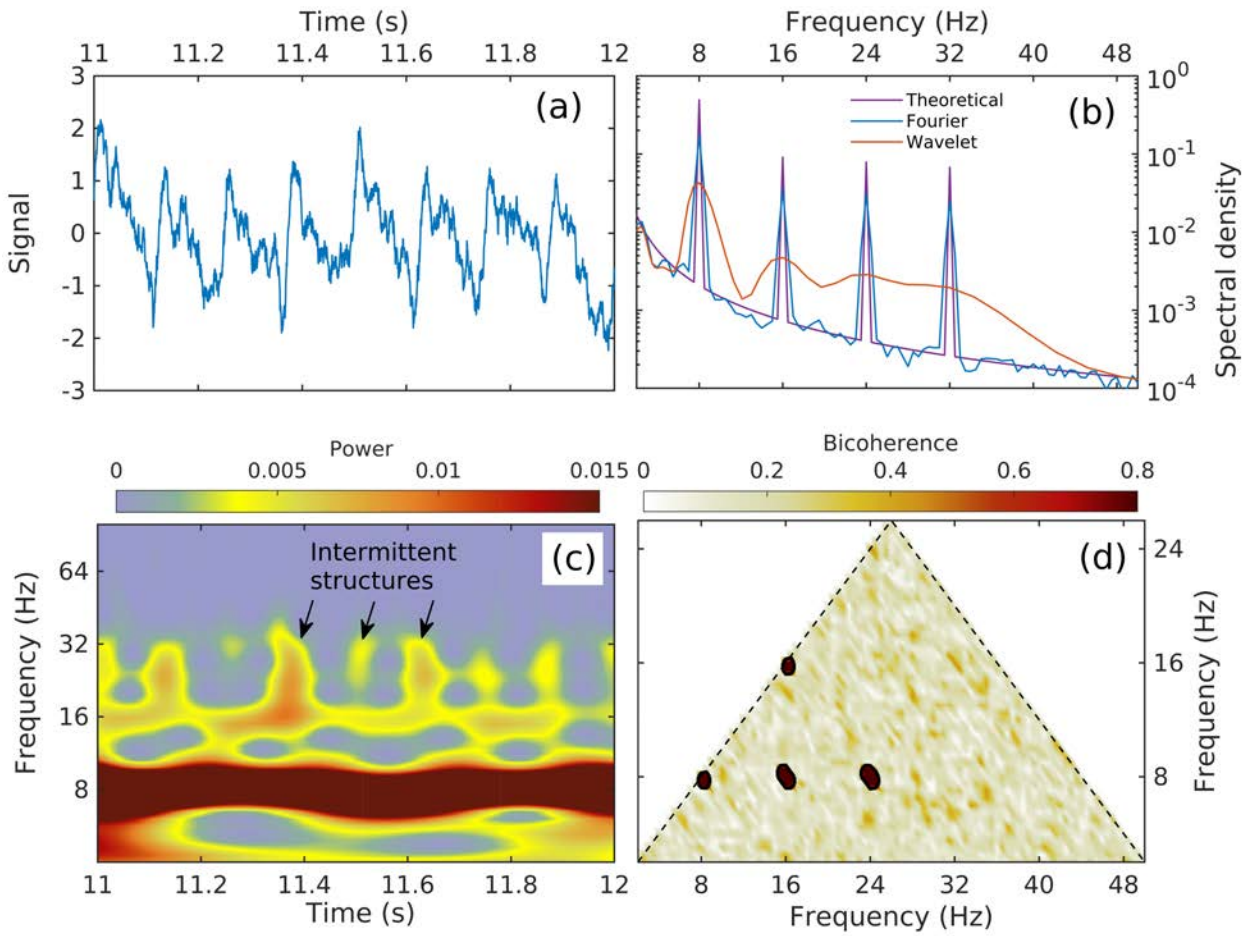

FIGURE 9. Example of Fourier and wavelet analysis of a synthetic time series emulating an LFP recording dominated by an asymmetric theta signal. The signal is constructed from an asymmetric sine function (an 8-Hz fundamental oscillation with phase-coupled harmonics), and pink ($f^{-1.5}$) noise. a) A time-series segment. b) Estimates of power spectral density. c) Scalogram. d) Bicoherence.

a spectral analysis tool for visual and auditory oscillations, hippocampal rhythms and time series data collected via imaging approaches [Daugman, 1980, Jones and Palmer, 1987, Klimesch, 1996, Engel et al., 2001, Buzsáki and Draguhn, 2004, Huupponen et al., 2006, Sheremet et al., 2018]. With its ability to resolve time-localized activity bursts, the wavelet transform has provided insight into the complex behavior of neural systems at different levels: from the microscopic dynamics of individual cells (e.g., analysis of intracellular recordings) [Tychinskii, 2001, Sosnovtseva et al., 2005, Pavlov et al., 2006] to the macroscopic level of widespread neuronal networks (e.g., analysis of EEG and MEG recordings) [Durka et al., 2002, Bosnyakova et al., 2006, Sitnikova et al., 2009].

We used carefully collected and classified LFP data to highlight the advantages and disadvantages of each analysis approach. The Fourier representation is better suited for stationary time series in which the Fourier components are at most weakly correlated (phase coupled). In this case,

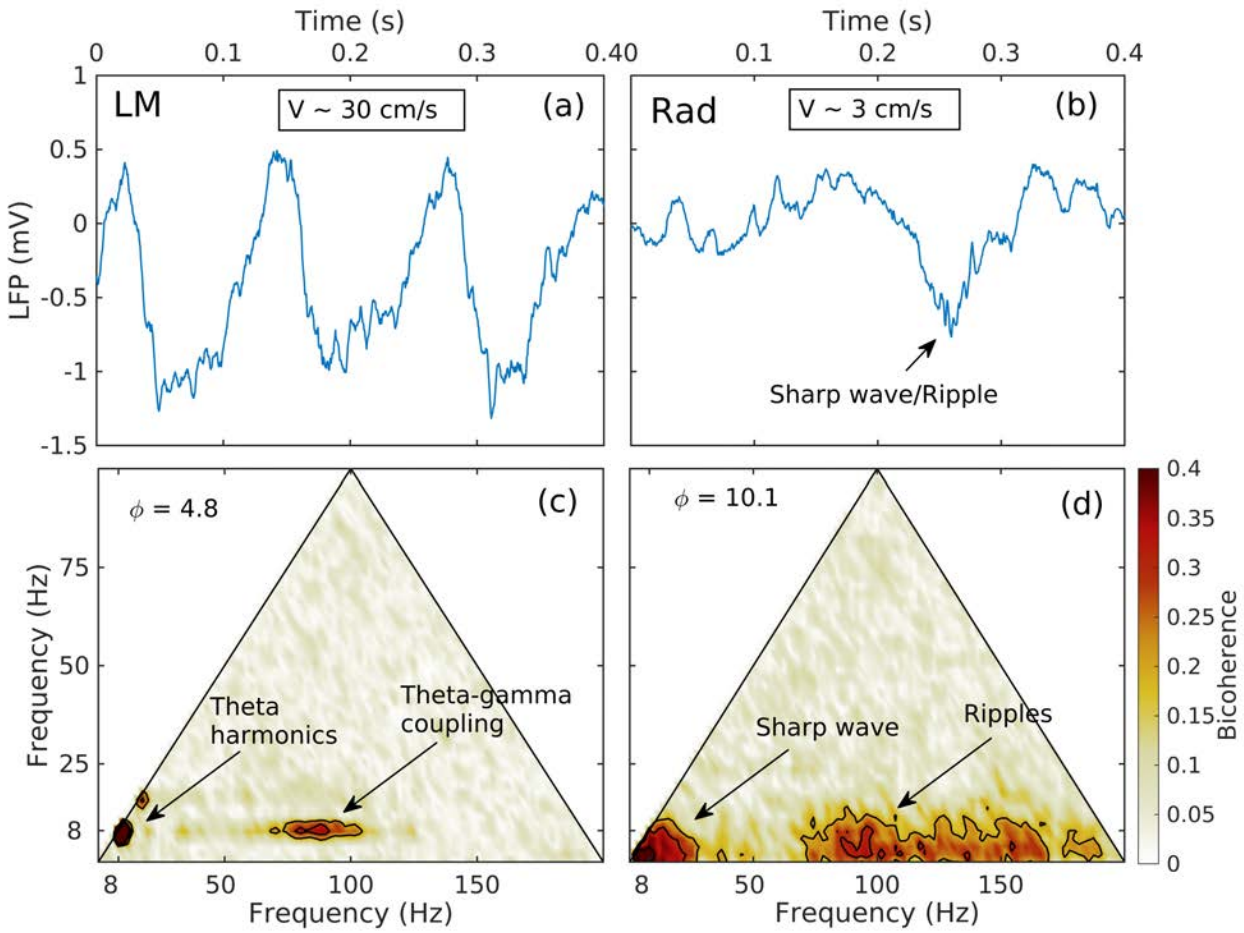

FIGURE 10. Examples of bicoherence estimates (c, d) for two LFP recordings (sample time series shown in panels a,b). Left: LM layer, active exploration at high speed motion; arrows mark the areas in the bicoherence map corresponding to theta/harmonics, and theta/gamma phase-coupling. Right: Rad layer, non-REM sleep; arrows mark the areas in the bicoherence map corresponding to the phase-coupling between Fourier components that assemble together into the solitary wave, and those that correspond to sharp wave and sharp-wave/ripples phase coupling (see also discussion in text).

there exists a stochastic process model that guaranties that averaged quantities exist, and provides the interpretation, for example, the spectral density represents the distribution of variance on each of the Fourier components. The wavelet transform is better suited for non-stationary, transient time series. No widely accepted stochastic model exists, that would provide the meaning of averaged wavelet analysis quantities.

The results of both the Fourier and wavelet representations become difficult to interpret when they are applied outside of their intended purpose. For example, the Fourier transform requires a very wide spectrum (for which the wavelet decomposition is better suited). Alternatively, when applied to a stationary time series that are best characterized using the Fourier transform, the wavelet transform shows fine two-dimensional details that are difficult to interpret (essentially

meaningless). Most importantly, the two transforms are not interchangeable, in the sense that the interpretation of results does not translate between the two transforms. This should not surprise: the commonly-used scale-frequency mapping is a deceiving device and should be used with great care. For example, to analyze a given signal, one could pick any of the orthogonal (or not) expansions available (e.g., Chebyshev, Bessel, Mellin, and so on – the list is very long, if not infinite); one could then associate in some way a unique frequency to the basis functions, and plot the coefficients squared of the expansion vs the assigned frequencies. Such a power spectral density representation would be a legitimate representation, but it should be clear that it would have very little to do with the variance spectrum of the Fourier representation.

Of course, data does not come labeled as stationary or non-stationary. One is (and should be) free to improvise, but this should be done with care. We propose a simple measure for classifying time series as stationary or non-stationary, based on the strength of phase correlations exhibited by the bispectrum.

Returning to the hippocampal LFP analysis, the frequency range between the periodic theta rhythm and solitary sharp waves is a gray area, open to alternative interpretations. The amplitude of the hippocampal gamma [Stumpf, 1965, Buzsáki et al., 1983] is known to be coupled with the theta rhythm [Demiralp et al., 2007, Colgin et al., 2009]. This cross-frequency interaction is believed to facilitate memory consolidation and recall, and can be modeled with quasi-stationary cross-frequency coupling, where theta and gamma form a interaction triad with the envelope of gamma groups modulated by theta [Sheremet et al., 2018]. Alternatively, several studies have suggested the neural activity in gamma frequency ranges may come in small packets, or bursts, rather then being rhythmical [Tallon-Baudry and Bertrand, 1999, Lundqvist et al., 2016].

Our results confirm the relationship between the strength of theta/harmonics phase coupling Scheffer-Teixeira and Tort, 2016 and increased rat speed, correlated to spatial navigation and memory consolidation [Winson, 1978, Seidenbecher et al., 2003, Buzsáki, 2005]. The theta/harmonics complex occupies the frequency range attributed also to the “low gamma” [Colgin et al., 2009, Canolty and Knight, 2010, Bieri et al., 2014]. Our wavelet analysis does indeed exhibit the type of behavior (intermittency in the scalogram plots, wide peaks in the wavelet power spectral densities) that lead to this attribution; however, we believe there are reasons to question the “low gamma” interpretation of these results. Still, in principle, it is quite possible that both the theta/harmonics complex and low gamma coexist in the 20 to 50 Hz frequency range.

This study suggests perhaps, a more general conclusion. Referring back to what we call the “associative approach” for studying the relationship between brain activity and cognitive behavior, it should be quite clear that, past a certain boundary, associations become a rather sterile game. Powerful data analysis techniques, used or misused, will generate ever finer, multi-dimensional features and details. As we increase our details in the the levels of analysis, steps need to be taken

to carefully interpret and describe the results in the context of a quantitative brain models. We hope to take up this issue in a subsequent paper.

APPENDIX A. SUBJECTS, SURGERY, NEUROPHYSIOLOGY

A.1. **Subjects and behavioral training.** All behavioral procedures were performed in accordance with the National Institutes of Health guidelines for rodents and with protocols approved by the University of Florida Institutional Animal Care and Use Committee. A total of five 4-10 months old Fisher344-Brown Norway Rats (Taconic) were used in the present study. This was a mixed sex cohort comprised of r530♂, r538♂, r539♀, r544♀, r695♀in order to integrate sex a biological variable and begin to alleviate the disparity in research focused exclusively on males [Clayton, 2015]. Upon arrival, rats were allowed to acclimate to the colony room for one week. The rats were housed and maintained on a 12:12 light/dark cycle. All training sessions and electrophysiological recordings took place during the dark phase of the rats' light/dark cycle. Training consisted of shaping the rats to traverse a circular track for food reward (45mg, unflavored dustless precision pellets; BioServ, New Jersey; Product #F0021). During this time, their body weight was slowly reduced to 85% to their arrival baseline. Once the rat reliably performed more than one lap per minute, they were implanted with a custom single shank silicon probe from NeuroNexus (Ann Arbor, MI). This probe was designed such that thirty-two recording sites, each with a recording area of 177 µm, were spaced 60 µm apart allowing incremental recording across the hippocampal lamina. In preparation for surgery, the probe was cleaned in a 4% dilution of Contrad detergent (Decon Contrad 70 Liquid Detergent, Fisher Scientific) and then rinsed in distilled water [Marie Vandecasteele et al., 2012].

A.2. **Surgical procedures.** Surgery and all other animal care and procedures were conducted in accordance with the NIH Guide for the Care and Use of Laboratory Animals and approved by the Institutional Animal Care and Use Committee at the University of Florida. Rats were initially sedated in an induction chamber. Once anesthetized, the rat was transferred to a nose cone. The head was shaved with care taken to avoid the whiskers. The rat was then transferred to the stereotax, gently securing the ear bars and placing the front teeth over the incisor bar. The stereotaxic nose cone was secured, ensuring that the rat was appropriately inhaling the anesthesia. During surgical implantation, the rats were maintained under anesthesia with isoflurane administered at doses ranging from 0.5 to 2.5%. Next, ophthalmic ointment was applied and tanning shades, fabricated out of foil, were placed over but not touching the eyes to minimize direct light exposure. Multiple cycle of skin cleaning, using betadine followed by alcohol was applied prior to the first incision from approximately the forehead to just behind the ears. The remaining fascia was blunt dissected away and bone bleeding was mitigated through application of bone wax or cautery. Once the location of bregma was determined, the site of the craniotomy was located and a 3x3mm contour was drilled out, but not completed. This was followed by the placement of 7 anchor screws in the bone as well

as a reference over the cerebellum and ground screw placed over the cortex. Once the screws were secured, a thin layer of dental acrylic (Grip Cement Industrial Grade, 675571 (powder) 675572 (solvent); Dentsply Caulk, Milford, DE) was applied taking care to not obscure the craniotomy location. Finally, the craniotomy location was completed, irrigating and managing bleeding as necessary once the bone fragment was removed. Next a portion of the dura was removed, taking care to avoid damaging the vessels and the surface of the neocortex. Small bleeding was managed with saline irrigation and gel foam (sterile absorbable gelatin sponges manufactured by Pharmacia & Upjohn Co, Kalamazoo, MI; a division of Pfizer, NY, NY). The probe implant coordinates targeted the dorsal hippocampus (AP: -3.2 mm, ML: 1.5 relative to bregma, DV: -3.7 to brain surface).

Once the probe was in place, the craniotomy was covered with silastic (Kwik-Sil, World Precision Instruments, Sarasota, FL) and then secured to the anchor screws with dental acrylic. Four copper mesh flaps were placed around the probe providing protection as well as acting as a potential Faraday cage. The wires from the reference and ground screws were soldered to the appropriate pins of the connector. Adjacent regions of the copper-mesh flaps were soldered together to ensure their electrical continuity and the ground wire soldered to the copper mesh taking care to isolate the reference from contact with the ground. Once the probe was secured, the rat received 10cc of sterile saline as well as metacam (1.0 mg/kg) subcutaneously (the non-steroidal anti-inflammatory is also known as meloxicam; Boehringer Ingelheim Vetmedica, Inc., St. Joseph, MO). The rat was placed in a cage and monitored constantly until fully recovered. Over the next 7 days, the rat was monitored to ensure recovery and no behavioral anomalies. Metacam was administered the day fol- lowing surgery as well. Antibiotics (Sulfamethoxazole/Trimethoprim Oral Suspension at 200mg/40mg per 5 mls; Aurobindo Pharma USA, Inc., Dayton, NJ) were administered in the rat mash for an additional 5 days.

A.3. **Neurophysiology.** Following recovery from surgery, rats were retrained to run unidirectionally on a circle track (outer diameter: 115 cm, inner diameter: 88 cm), receiving food reward at a single location. For rats 530, 544 and 695, data is only analyzed from the circle track conditions. In order to deal with low velocities from the circle track datasets, additional datasets for rats 538 and 539 from running on figure-8 track (112 cm wide x 91 cm length) were used. In this task, rats were rewarded on successful spatial alternations. Only datasets in which the rats performed more than 85% of trials correctly were used. The local-field potential was recorded on a Tucker-Davis Neurophysiology System (Alachua, FL) at ~24 kHz (PZ2 and RZ2, Tucker-Davis Technologies). The animal's position was recorded at 30 frames/s (Tucker-Davis). Spatial resolution was less than 0.5 cm/pixel.

Speed was calculated as the smoothed derivative of position. The local-field potential data was analyzed in Matlab® (MathWorks, Natick, MA, USA) using custom written code as well as code imported from the HOSAtoolbox [Swami et al., 2001]. Raw LFP records sampled at 24 kHz

(Tucker-Davis system) were low-pass filtered down to 2 kHz and divided into fragments of 2048 time samples (approximately 1 second).

APPENDIX B. FOURIER AND WAVELET TRANSFORMS

B.1. **Transforms.** The Fourier and wavelet transforms can be introduced formally as decomposition on an orthogonal basis. Let $\mathcal{S}$ be some class of real functions and let ψ_f ($f \in \mathbb{R}$) be a basis in $\mathcal{S}$; then any $g \in \mathcal{S}$ can be written uniquely as

$$G(t) = \int g(t)\psi_f^*(t)dt,\ g(t) = \int G(f)\psi_f(t)df. \tag{2}$$

The "coefficients" $G(f)$ of the decomposition (also referred to as the transform of g) are obtained by taking the inner product of the function g with the basis elements (i.e., projecting $g(t)$ onto the basis), The pair of equations 2 are best known as direct and inverse transforms, sometimes also called analysis and synthesis.

The Fourier transform pair is obtained letting $\psi_f(t) = e^{2\pi i f t}$

$$G(f) = \int_{-\infty}^{\infty} g(t)e^{-2\pi i f t}dt,\ g(t) = \int_{-\infty}^{\infty} G(f)e^{2\pi i f t}df. \tag{3}$$

Unless the set of functions is carefully defined, equations 3 are only formal, and in most cases they do not have any elementary mathematical meaning; when they do, their usefulness is limited. For example, if $g(t) = 1$, the Riemann integral in equation 3 does not exist; however, a rather restrictive elementary theory can be built for T-periodic functions.

The wavelet transform and its inverse are given by

$$G(s,\tau) = \int_{-\infty}^{\infty} g(t)\psi_{s\tau}(t)dt,\ g(t) = \iint_{-\infty}^{\infty} G(s,\tau)\psi_{s\tau}(t)dsd\tau \tag{4}$$

where the functions $\psi_{s,\tau}(t) = \alpha\varphi\left(\frac{t-\tau}{s}\right)$ are "copies" of the "mother wavelet" $\varphi(t)$, shifted in time by τ and scaled by s, with α a normalization constant. The full set of wavelets $\{\psi_{s,\tau}(t)\}_{s,\tau\in\mathbb{R}}$ is in general complete but not independent (i.e., larger than a basis).

B.1.1. *Discrete transforms.* Evolving the generic equations 3 and 4 into useful analysis tools has complexities that required the development of full theories (e.g., the theory of distributions, or generalized functions, e.g., Schwartz 1950, 1951, Lighthill 1958). For example, in equations 3, $\psi_f(t) = e^{2\pi i f t}$ are orthogonal in the sense that $\int_{-\infty}^{\infty} e^{2\pi i f t}dt = \delta(f)$, where δ is the Dirac function Strichartz [1994], Vladimirov [2002]. A complete discussion of these is far beyond the scope of this study, and is also unnecessary, because time series measured in practical applications are always of finite length T, sampled at time intervals Δt ($T = n\Delta t$), i.e., are finite sequences of real numbers $g(t) = \{g_1, g_2, \cdots, g_N\}$, with $g_j = g(t_j)$. Such sequences naturally form N-dimensional spaces, in which integral transforms equations 2-**??** (e.g., Fourier, or wavelet transforms) are represented by finite-dimensional linear operators, i.e., $N \times N$ matrices. These discretized versions

of the Fourier and wavelet representations are called the *discrete* transforms [Strang, 1986, Briggs and Henson, 1995, Mallat, 1998].

The discrete Fourier transform pair is (in Matlab® convention)

$$G_m = \frac{1}{N}\sum_{n=0}^{N-1} g_n \psi_{mn},\ g_n = \sum_{m=0}^{N-1} G_m \psi^*_{mn},\ \psi_{mn} = e^{-2\pi i \frac{mn}{N}}, \tag{5}$$

where $\psi_{mn} = \psi_m(t_n) = e^{-2\pi i f_m t_n}$ are the basis vectors. The equations in the pair (5) are some times called the analysis and synthesis of the signal $g(t)$. Here, $f_m = m\Delta f$ and $t_n = n\Delta t$ represent the discretized frequency and time grids, with $\Delta f = \frac{1}{T}$, and $\Delta t = \frac{T}{N}$. Basis functions are orthogonal in the sense that, for any integer m, with $m \neq 0$ and $m \neq N$, $\sum_{n=0}^{N-1} e^{-2\pi i \frac{mn}{N}} = 0$.

A discrete version of wavelet transform is

$$G_{mn} = \sum_{k=0}^{N-1} g_k \varphi_{mnk},\ \text{with } \varphi_{mnk} = s^{-\frac{m}{2}} \varphi\left[s^{-m}\left(k - n\Delta\tau s^m\right)\right], \tag{6}$$

where $\Delta\tau$ is a time-shift increment. The wavelets φ_{mnk} form orthogonal only for compact-support wavelet shapes φ (e.g., Haar, and Daubechies wavelets) [Daubechies, 1988, 1992, Mallat, 1998].

The Parseval relation insures that equations 5 conserve the variance of the time sequence and its transform [e.g., Briggs and Henson, 1995], i.e., $\sigma^g = \sigma^G$, where $\sigma^g = \sum_n |g_n|^2$ is the variance of g. The discrete wavelet transform does conserve variance ($\sigma^g \neq \sigma^G$) and in general, the variance ratio depends on g, which means that a universal correction factor does not exist.

B.1.2. *Time-frequency atoms.* For the Fourier transform 5, the duration T of the time sequence and the frequency resolution Δf of the transformed sequence are related through the reciprocity relation

$$T\Delta f = 1, \tag{7}$$

which implies that increasing the frequency resolution Δf is equivalent to increasing the time duration T of the analyzed signal. Equation 7 highlights an important limitation of the Fourier transform: if $g(t)$ is highly localized, its transform $G(f)$ has a wide frequency support. This means that very high sampling rates to cover the wide frequency domain, and the interpretation of the high-frequency content can become difficult. Restricting the Fourier analysis equation 3 to a specified duration T is equivalent to multiplying the time series $g(t)$ by finite support rectangular window $w(t-\tau) = 1$ if $|t-\tau| \leq T/2$ and zero otherwise,

$$\int_{\tau-T/2}^{\tau+T/2} dt e^{-2\pi i f t} = \int_{\tau-T/2}^{\tau+T/2} dt\, w(t-\tau)\, e^{-2\pi i f t} = \int_{-\infty}^{\infty} dt \varphi^*_{f\tau}(t), \tag{8}$$

or, alternatively by projecting g onto functions $\varphi(t) = w(t)\psi(t)$. The function φ could be described as a localized oscillation. If one constructs in the time-frequency plane a rectangle of sides

T and Δf centered, say, at $t_0 = \frac{T}{2}$ and $f_0 = \frac{T\Delta f}{2\Delta t}$, equation 7 states that the area of this rectangle is constant, regardless of the value of T. This rectangle is sometimes called Heisenberg box [Mallat, 1998]. Equation 7 is in fact an example of the application of the general Heisenberg uncertainty principle, which states that the area of a Heisenberg box cannot be made arbitrarily small. For an arbitrarily-shaped localized oscillation $\varphi(t)$ with Fourier transform $\phi(f)$ and unit variance ($\int_{-\infty}^{\infty} |\varphi|^2 \, dt = \int_{-\infty}^{\infty} |\phi|^2 \, dt = 1$), defining the time and frequency widths as

$$\sigma_t = \int_{-\infty}^{\infty} (t - t_0)^2 \, |\varphi|^2 \, dt, \quad \sigma_f = \int_{-\infty}^{\infty} (f - f_0)^2 \, |\phi|^2 \, dt, \tag{9}$$

one can show [Gabor, 1946, Mallat, 1998, Percival and Walden, 2009] that

$$\sigma_t \sigma_f \geq \frac{1}{4\pi}. \tag{10}$$

In other words, it is impossible to achieve simultaneous arbitrary resolutions both in time and frequency.

While the time-frequency resolution (area of Heisenberg boxes) cannot be made arbitrarily small, it can be minimized. [Gabor, 1946] showed that the minimal area for a Heisenberg box is achieved by localized oscillation $\varphi(t) = w(t)e^{2\pi i f t}$ where w is a a Gaussian-shaped window. Following his work, [Goupillaud et al., 1984] and [Goupillaud et al., 1984] used this shape, later called the Morlet wavelet, to introduce the continuous wavelet transform [Grossmann and Morlet, 1984, Mallat, 1998] The limitations imposed by the Heisenberg uncertainty principle are illustrated in figure 11. A Morlet wavelet results as a product of a sine function with a Gaussian window (figure 11, a-b). The resulting function is the "mother wavelet" (figure 11, c). The wavelet transform thens uses scaled versions of the mother wavelet (figure 11, d) as "elementary" functions. It is important to note that the wavelets shown in figure 11, panel d, are not harmonic, therefore they are *not uniquely characterized by a single frequency value*; instead, the are characterized by a frequency interval, say, corresponding to the width of the frequency spread of their power (as given by the Fourier transform). The frequency distribution of power is, as expected, narrower for the larger-scale wavelets, and wider for smaller-scale wavelets (figure 11, e). Therefore the wavelet Heisenberg boxes coverage of the frequency axis is not-uniform (figure 11, f), and consequently, using wavelets as a "frequency" representation results in a non-uniform frequency resolution, with resolution degrading at higher frequencies.

Treating the wavelet transform as a frequency decomposition amounts to assigning a unique frequency to each wavelet scale, in effect transforming the dual space from "scale space" to a "frequency space". In the case of the Morlet wavelet, because the Gaussian is self-similar under the Fourier transform, the frequency distribution of the wavelet is also a Gaussian, is symmetric and has a maximum, therefore it seems logical to choose the peak frequency as the nominal frequency. It should be clear that this scale-to-frequency transformation is arbitrary in the general case and most likely meaningless.

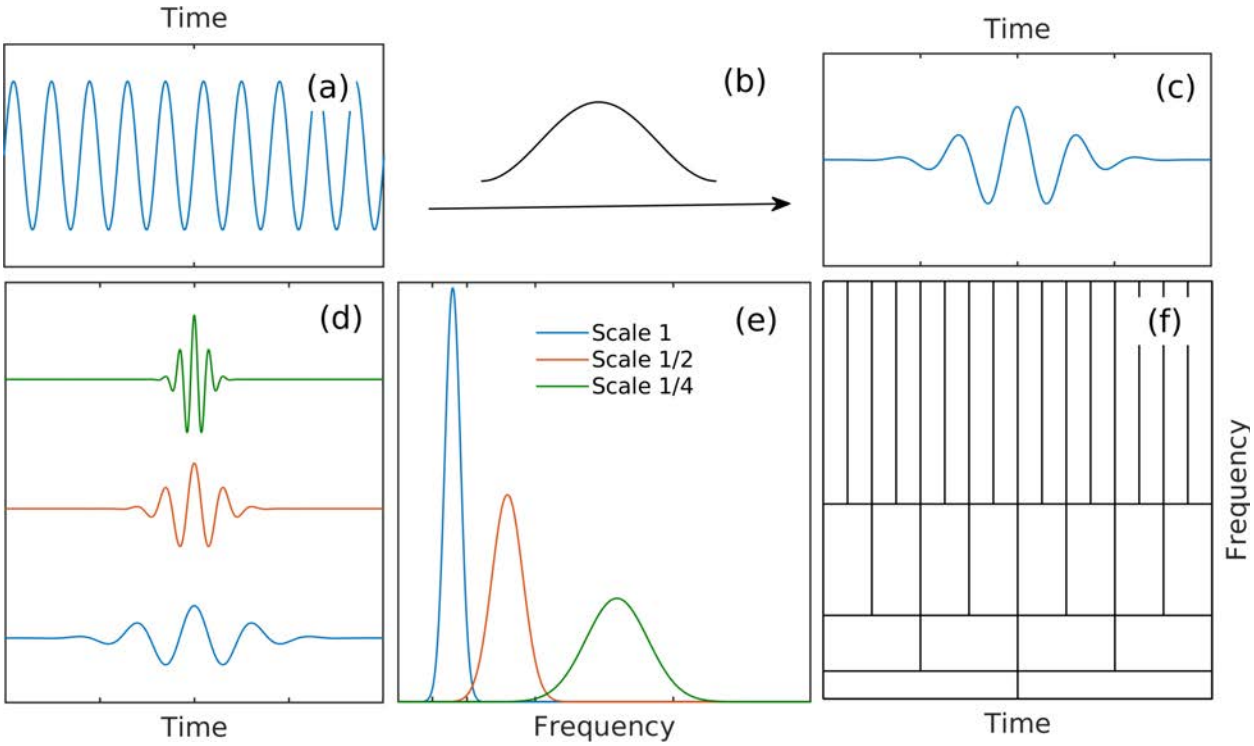

FIGURE 11. A schematic of the Heisenberg boxes of the wavelet transform. The mother wavelet is obtained by the multiplication of a sine function with a window (panels a-c). d) Wavelets at three scales resulting by the scaling of the mother wavelet. e) Frequency distribution of the power of wavelets shown in e). f) Heisenberg boxes of the wavelet transform.

B.2. **Spectral analysis.** The spectral analysis of the LFP in the current study was based on standard techniques used for stationary signals [Priestley, 1981, Papoulis and Pillai, 2002] as previously described in [Sheremet et al., 2016a]. Assume the LFP recordings $g(t)$ and $h(t)$ are realizations of zero-mean stochastic processes, stationary in the relevant statistics, with Fourier transforms $G(f_n)$ and $H(f_n)$, $n = 1, \cdots, N$. The second and third order spectral statistics are estimated using cross-spectrum and bispectrum, defined as

$$S_n^{gh} = S^{gh}(f_n) = \langle G_n H_n^* \rangle, \tag{11}$$

$$B_{mn} = B(f_m, f_n) = \left\langle G_m G_n G_{m+n}^* \right\rangle. \tag{12}$$

where the angular brackets denote the ensemble average, the asterisk denotes complex conjugation, and we omit the superscript when a single time series is involved. The diagonal $S_n^{g,g}$ of the cross-spectrum matrix are power spectra. The coherence and phase lag of time series g and h are the normalized modulus and phase of the cross-spectrum,

$$C_n^{gh} = \frac{S^{gh}(f_n)}{\sqrt{S_n^{gg} S_n^{hh}}}, \text{ and } \Theta_n^{gh} = \arg S^{gh}(f_n) \tag{13}$$

The cross-spectrum matrix provides information about the degree of correlation and phase lags for between different time series; spectra describe the frequency distribution of the variance of processes g and h, i.e., a complete characterization of the average linear structure of the Fourier representation.

The bispectrum provides information about the phase correlations between different frequency components of the same time series (e.g., Sheremet et al., 2016a, Kovach et al., 2018). The bispectrum is statistically zero if the Fourier coefficients are mutually independent, i.e., for a linear system. The bispectrum will exhibit peaks at triads (f_n, f_m, f_{n+m}) that are phase correlated. The real and imaginary part of the bispectrum are related to the skewness γ and asymmetry α of the time series g through

$$\sigma^{-3} \sum_{m,n} B_{mn} = \gamma + i\alpha, \tag{14}$$

where σ is its standard deviation [Masuda and Kuo, 1981, Haubrich and MacKenzie, 1965]. The bicoherence b_{mn} and biphase Φ_{mn} are defined in way similar to the coherence and phase lag as the normalized modulus and the argument of the bispectrum, that is

$$b_{mn} = \frac{B_{mn}}{\sqrt{S_m S_n S_{m+n}}}, \text{ and } \Phi_{mn} = \arg B_{mn}. \tag{15}$$

B.2.1. *Phase-coupling measure.* The phase-coupling measure is defined as the square root of the bicoherence integrated over the frequency domain of interest [Sheremet et al., 2002]:

$$\phi = \left(\sum_{m,n \in I} b_{mn} - \frac{1}{2} \sum_{m} b_{mm} \right) (\Delta f)^2 , \tag{16}$$

where the discrete two-dimensional interval I is typically defined as all the indices in the bispectrum triangle, i.e., pairs of integer indices (m, n), such that $1 \leq m \leq N$ and $1 < n \leq \min(m, N - m + 1)$; due to the symmetries of the bispectrum, diagonal terms should be halved.

The proposed measure 16 is not independent of frequency resolution and and number of realizations used, therefore the interpretation is somewhat loose: one should exercise care and discernment using it. Figure 12 illustrates this idea.

B.3. **Numerical implementation.** Fourier and wavelet analysis procedures were implemented in the Matlab® environment using available Matlab® toolboxes. The Fourier cross-spectrum was estimated by dividing the LFP time series into 2000-point (1 second) segments sorted by rat speed and windowed using a hamming window; cross-spectra were estimated by averaging over all segments in each speed bin. The wavelet transform used the Morlet wavelet, with the central frequency of Morlet wavelet used as nominal frequency.

The wavelet scalogram is defined as the logarithm of the squared modulus $|G_{mn}|^2$ of the wavelet coefficients (equation 6). The power spectral density for the wavelet transform is computed as the

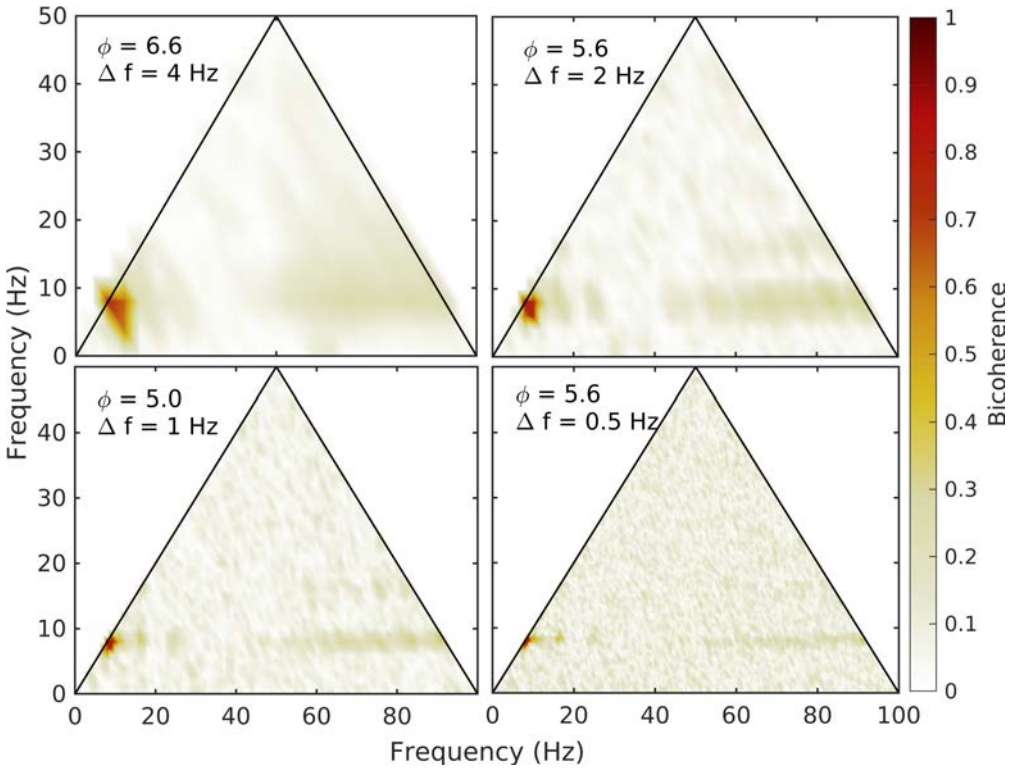

FIGURE 12. Illustration of the stability of the phase coupling measure ϕ (equation 16) applied to a 100-s LFP recording (LM layer) sampled at 2000 Hz, for four frequency resolutions Δf. Data are obtained from r530♂.

time marginal of the wavelet transform [Abry et al., 1993]. The Fourier spectra are estimated using the Welch method [Welch, 1967].

CONFLICT OF INTEREST STATEMENT

The authors declare that the research was conducted in the absence of any commercial or financial relationships that could be construed as a potential conflict of interest.

AUTHOR CONTRIBUTIONS

AM and AS developed the concept, methodology, part of the Matlab® tools, and supervised and guided the research. JK performed the surgery and led the data collection effort. YZ participated in the data collection and analyzing processing. AM, AS and YZ worked together in analysis, interpretation, literature research and writing.

FUNDING

This work was supported by the McKnight Brain Research Foundation, and NIH grants- Grant Sponsor: National Institute on Aging; Grant number: AG055544 and Grant Sponsor: National Institute on Mental Health; Grant Number: MH109548.

ACKNOWLEDGMENTS

This work was supported by the McKnight Brain Research Foundation, and NIH grants- Grant Sponsor: National Institute on Aging; Grant number: AG055544 and Grant Sponsor: National Institute on Mental Health; Grant Number: MH109548. Special thanks to S.D. Lovett for technical support, and Yu Qin for insightful discussions.

DATA AVAILABILITY STATEMENT

The datasets for this manuscript are not publicly available because these data are part of ongoing student dissertation research. Requests to access the datasets should be directed to either Alex Sheremet (alex.sheremet@essie.ufl.edu) or Drew Maurer (drewmaurer@ufl.edu).

REFERENCES

Patrice Abry, Paulo Gonçalves, and Patrick Flandrin. Wavelet-based spectral analysis of 1/f processes. In *Acoustics, Speech, and Signal Processing, 1993. ICASSP-93., 1993 IEEE International Conference on*, volume 3, pages 237–240. IEEE, 1993. B.3

O.J. Ahmed and M.R. Mehta. Running speed alters the frequency of hippocampal gamma oscillations. *Journal of Neuroscience*, 32:7373–7383, 2012. 1

I. Antoniou and K. Gustafson. Wavelets and stochastic processes. *Mathematics and Computers in Simulation*, 49:81–104, 1999. 3.3.2

Mariano A Belluscio, Kenji Mizuseki, Robert Schmidt, Richard Kempter, and György Buzsáki. Cross-frequency phase–phase coupling between theta and gamma oscillations in the hippocampus. *Journal of Neuroscience*, 32(2):423–435, 2012. 1

Kevin Wood Bieri, Katelyn N Bobbitt, and Laura Lee Colgin. Slow and fast gamma rhythms coordinate different spatial coding modes in hippocampal place cells. *Neuron*, 82(3):670–681, 2014. 1, 4

Daria Bosnyakova, Alexandra Gabova, Galina Kuznetsova, Yuri Obukhov, Inna Midzyanovskaya, Dmitrij Salonin, Clementina van Rijn, Anton Coenen, Leene Tuomisto, and Gilles van Luijtelaar. Time–frequency analysis of spike-wave discharges using a modified wavelet transform. *Journal of neuroscience methods*, 154(1-2):80–88, 2006. 4

ANATOL Bragin, G Jando, Z Nadasdy, M Van Landeghem, and G Buzsáki. Dentate EEG spikes and associated interneuronal population bursts in the hippocampal hilar region of the rat. *Journal of Neurophysiology*, 73(4):1691–1705, 1995a. 2.2, 3.2

Anatol Bragin, Gábor Jandó, Zoltán Nádasdy, Jamille Hetke, K Wise, and Gy Buzsáki. Gamma (40-100 Hz) oscillation in the hippocampus of the behaving rat. *Journal of Neuroscience*, 15(1): 47–60, 1995b. 1

Anatol Bragin, Gábor Jandó, Zoltán Nádasdy, Jamille Hetke, K Wise, and Gy Buzsáki. Gamma (40-100 Hz) oscillation in the hippocampus of the behaving rat. *Journal of Neuroscience*, 15(1): 47–60, 1995c. 2.1

W. L. Briggs and V. E. Henson. *The DFT: An Owner's Manual for the Discrete Fourier Transform*. SIAM - Society for Industrial and Applied Mathematics, 1995. B.1.1, B.1.1

G. Buzsaki. Hippocampal sharp waves: their origin and significance. *Brain Research*, 398:242–252, 1986. 1

G. Buzsaki. Hippocampal sharp wave-ripple: A cognitive biomarker for episodic memory and planning. *Hippocampus*, 25(10):1073–1188, 2015. 2.2

G. Buzsaki, W.L. Leung, and C.H. Vanderwolf. Cellular bases of hippocampal EEG in the behaving rat. *Brain Research*, 287:139–171, 1983. 2.2

Gy Buzsáki, J Czopf, I Kondakor, and L Kellenyi. Laminar distribution of hippocampal rhythmic slow activity (RSA) in the behaving rat: current-source density analysis, effects of urethane and atropine. *Brain research*, 365(1):125–137, 1986. 2.1, 2.1

György Buzsáki. Theta rhythm of navigation: link between path integration and landmark navigation, episodic and semantic memory. *Hippocampus*, 15(7):827–840, 2005. 1, 4

György Buzsáki. Hippocampal sharp wave-ripple: A cognitive biomarker for episodic memory and planning. *Hippocampus*, 25(10):1073–1188, 2015. 3.2

György Buzsáki and Andreas Draguhn. Neuronal oscillations in cortical networks. *science*, 304 (5679):1926–1929, 2004. 4

György Buzsáki, Cornelius H Vanderwolf, et al. Cellular bases of hippocampal EEG in the behaving rat. *Brain Research Reviews*, 6(2):139–171, 1983. 1, 2.1, 4

Ryan T Canolty and Robert T Knight. The functional role of cross-frequency coupling. *Trends in cognitive sciences*, 14(11):506–515, 2010. 4

Margaret F Carr, Mattias P Karlsson, and Loren M Frank. Transient slow gamma synchrony underlies hippocampal memory replay. *Neuron*, 75(4):700–713, 2012. 1

Z. Chen, E. Resnik, J.M. McFarland, B. Sakmann, and M.R. Mehta. Speed controls the amplitude and timing of the hippocampal gamma rhythm. *PLoS One*, 6:e21408, 2011. 1

Janine Austin Clayton. Studying both sexes: a guiding principle for biomedicine. *The FASEB Journal*, 30(2):519–524, 2015. A.1

AML Coenen. Frequency analysis of rat hippocampal electrical activity. *Physiology & Behavior*, 14(3):391–394, 1975. 3.1.1

Laura Lee Colgin. Do slow and fast gamma rhythms correspond to distinct functional states in the hippocampal network? *Brain research*, 1621:309–315, 2015. 1

Laura Lee Colgin, Tobias Denninger, Marianne Fyhn, Torkel Hafting, Tora Bonnevie, Ole Jensen, May-Britt Moser, and Edvard I Moser. Frequency of gamma oscillations routes flow of information in the hippocampus. *Nature*, 462(7271):353, 2009. 1, 3.1.1, 4

Jozsef Csicsvari, Hajime Hirase, András Czurkó, Akira Mamiya, and György Buzsáki. Oscillatory coupling of hippocampal pyramidal cells and interneurons in the behaving rat. *Journal of Neuroscience*, 19(1):274–287, 1999. 2.1

I. Daubechies. *Ten lectures on wavelets.* SIAM - Society for Industrial and Applied Mathematics, 1992. 6, B.1.1

Ingrid Daubechies. Orthonormal bases of compactly supported wavelets. *Communications on pure and applied mathematics*, 41(7):909–996, 1988. B.1.1

John G Daugman. Two-dimensional spectral analysis of cortical receptive field profiles. *Vision research*, 20(10):847–856, 1980. 4

Tamer Demiralp, Zubeyir Bayraktaroglu, Daniel Lenz, Stefanie Junge, Niko A Busch, Burkhard Maess, Mehmet Ergen, and Christoph S Herrmann. Gamma amplitudes are coupled to theta phase in human EEG during visual perception. *International journal of psychophysiology*, 64 (1):24–30, 2007. 4

Piotr J Durka, Waldemar Szelenberger, Katarzyna J Blinowska, Wojciech Androsiuk, and Maciej Myszka. Adaptive time–frequency parametrization in pharmaco EEG. *Journal of neuroscience methods*, 117(1):65–71, 2002. 4

S. Elgar. Relationships involving third moments and bispectra of a harmonic process. *IEEE transactions on Acoustics, Speech , and Signal Processing*, ASSP-35(12):1725–1726, 1987. 3.3.3

Andreas K Engel, Pascal Fries, and Wolf Singer. Dynamic predictions: oscillations and synchrony in top–down processing. *Nature Reviews Neuroscience*, 2(10):704, 2001. 4

Oxana Eschenko, Wiam Ramadan, Matthias Mölle, Jan Born, and Susan J Sara. Sustained increase in hippocampal sharp-wave ripple activity during slow-wave sleep after learning. *Learning & Memory*, 15(4):222–228, 2008. 2.2, 3.2

G.T. Fechner. *Elemente der Psychophysik*. Breitkopf und Härtel, 1860. 2.2

Pascal Fries, John H Reynolds, Alan E Rorie, and Robert Desimone. Modulation of oscillatory neuronal synchronization by selective visual attention. *Science*, 291(5508):1560–1563, 2001. 1

D. Gabor. Theory of Communication. *Journal of Institution of Electrical Engineers*, 93(3):429–457, 1946. B.1.2, B.1.2

P. Goupillaud, A. Grossman, and J. Morlet. Cycle-octave and related transforms in seismic signal analysis. *Geoexploration*, 23:85–102, 1984. B.1.2

John D Green and Arnaldo A Arduini. Hippocampal electrical activity in arousal. *Journal of neurophysiology*, 17(6):533–557, 1954. 1, 2.2

Andres D Grosmark, Kenji Mizuseki, Eva Pastalkova, Kamran Diba, and György Buzsáki. REM sleep reorganizes hippocampal excitability. *Neuron*, 75(6):1001–1007, 2012. 2.2

A. Grossmann and J. Morlet. Decomposition of Hardy functions into square integrable wavelets of constant shape. *Soc. Int. Am. Math. (SIAM), Journal of Mathematical Analysis*, 1984. B.1.2

RM Harper. Frequency changes in hippocampal electrical activity during movement and tonic immobility. *Physiology & behavior*, 7(1):55–58, 1971. 3.1.1

Richard A Haubrich and Glenn S MacKenzie. Earth noise, 5 to 500 millicycles per second: 2. Reaction of the Earth to oceans and atmosphere. *Journal of Geophysical Research*, 70(6):1429–1440, 1965. B.2

Eero Huupponen, Wim De Clercq, Germán Gómez-Herrero, Antti Saastamoinen, Karen Egiazarian, Alpo Värri, Bart Vanrumste, Anneleen Vergult, Sabine Van Huffel, Wim Van Paesschen, et al. Determination of dominant simulated spindle frequency with different methods. *Journal of neuroscience methods*, 156(1-2):275–283, 2006. 4

Judson P Jones and Larry A Palmer. An evaluation of the two-dimensional Gabor filter model of simple receptive fields in cat striate cortex. *Journal of neurophysiology*, 58(6):1233–1258, 1987. 4

Richard Jung and Alois E Kornmüller. Eine methodik der ableitung iokalisierter potentialschwankungen aus subcorticalen hirngebieten. *Archiv für Psychiatrie und Nervenkrankheiten*, 109(1):1–30, 1938. 1

Caleb Kemere, Margaret F Carr, Mattias P Karlsson, and Loren M Frank. Rapid and continuous modulation of hippocampal network state during exploration of new places. *PloS one*, 8(9): e73114, 2013. 1, 3.1

Wolfgang Klimesch. Memory processes, brain oscillations and EEG synchronization. *International journal of psychophysiology*, 24(1-2):61–100, 1996. 4

Christopher K Kovach, Hiroyuki Oya, and Hiroto Kawasaki. The bispectrum and its relationship to phase-amplitude coupling. *NeuroImage*, 173:518–539, 2018. 3.3.3, B.2

Lai-Wo Stan Leung, FH Lopes Da Silva, and WJ Wadman. Spectral characteristics of the hippocampal EEG in the freely moving rat. *Electroencephalography and clinical neurophysiology*, 54(2):203–219, 1982. 3.1.1

LS Leung. Nonlinear feedback model of neuronal populations in hippocampal CAl region. *Journal of Neurophysiology*, 47(5):845–868, 1982. 3.1.1

LW Leung. Model of gradual phase shift of theta rhythm in the rat. *Journal of Neurophysiology*, 52(6):1051–1065, 1984. 2.1

J. M. Lighthill. *An Introduction to Fourier Analysis and Generalised Functions* . Cambridge Monographs on Mechanics, 1958. B.1.1

John E Lisman and Marco A Idiart. Storage of 7+/-2 short-term memories in oscillatory subcycles. *Science*, 267(5203):1512–1515, 1995. 1

Mikael Lundqvist, Jonas Rose, Pawel Herman, Scott L Brincat, Timothy J Buschman, and Earl K Miller. Gamma and beta bursts underlie working memory. *Neuron*, 90(1):152–164, 2016. 4

S. Mallat. *A wavelet tour of signal processing*. Academic Press, San Diego, 1998. B.1.1, B.1.1, B.1.2, B.1.2, B.1.2

SM Marie Vandecasteele, Sébastien Royer, Mariano Belluscio, Antal Berényi, Kamran Diba, Shigeyoshi Fujisawa, Andres Grosmark, Dun Mao, Kenji Mizuseki, Jagdish Patel, et al. Large-scale recording of neurons by movable silicon probes in behaving rodents. *Journal of visualized experiments: JoVE*, (61), 2012. A.1

A. Masuda and Y.-Y. Kuo. A note on the imaginary part of bispectra. *Deep Sea Research*, 28(3): 213–222, 1981. B.2

A.P. Maurer, S. R. Vanrhoads, G.R. Sutherland, P. Lipa, and B.L. McNaughton. Self-motion and the origin of differential spatial scaling along the septo-temporal axis of the hippocampus. *Hippocampus*, 15:841–852, 2005. 2.2

Ulla Mitzdorf. Current source-density method and application in cat cerebral cortex: investigation of evoked potentials and EEG phenomena. *Physiological reviews*, 65(1):37–100, 1985. 2.1, 2.1

Sean M Montgomery and György Buzsáki. Gamma oscillations dynamically couple hippocampal CA3 and CA1 regions during memory task performance. *Proceedings of the National Academy of Sciences*, 104(36):14495–14500, 2007. 1

Sean M Montgomery, Martha I Betancur, and György Buzsáki. Behavior-dependent coordination of multiple theta dipoles in the hippocampus. *Journal of Neuroscience*, 29(5):1381–1394, 2009. 1

RGM Morris and JJ Hagan. Hippocampal electrical activity and ballistic movement. *Neurobiology of the hippocampus*, pages 321–331, 1983. 1, 3.1

John O'keefe and Lynn Nadel. *The hippocampus as a cognitive map*. Oxford: Clarendon Press, 1978. 1

A. Papoulis and S.U. Pillai. *Probability, random variables, and stochastic processes*. Tata McGraw-Hill Education, 2002. 3.3.2, B.2

Alexey N Pavlov, Valeri A Makarov, Erik Mosekilde, and Olga V Sosnovtseva. Application of wavelet-based tools to study the dynamics of biological processes. *Briefings in bioinformatics*, 7(4):375–389, 2006. 4

D. Percival and A. Walden. *Spectral Analysis for Physical Applications*. Cambridge, GBR: Cambridge University Press, 2009. 3.3.2, B.1.2

J.B. Priestley. *Spectral analysis and time series*. Academic Press, 1981. 3.3.2, 3.3.2, B.2

P Rappelsberger, H Pockberger, and H Petsche. Current source density analysis: methods and application to simultaneously recorded field potentials of the rabbit's visual cortex. *Pflügers Archiv*, 389(2):159–170, 1981. 2.1, 2.1

Robson Scheffer-Teixeira and Adriano BL Tort. On cross-frequency phase-phase coupling between theta and gamma oscillations in the hippocampus. *Elife*, 5:e20515, 2016. 1, 3.1, 4

L. Schwartz. *Théorie des distributions, Tome I*. Hermann, 1950. B.1.1

L. Schwartz. *Théorie des distributions, Tome II*. Hermann, 1951. B.1.1

Thomas Seidenbecher, T Rao Laxmi, Oliver Stork, and Hans-Christian Pape. Amygdalar and hippocampal theta rhythm synchronization during fear memory retrieval. *Science*, 301(5634): 846–850, 2003. 4

A Sheremet, RT Guza, Steve Elgar, and THC Herbers. Observations of nearshore infragravity waves: Seaward and shoreward propagating components. *Journal of Geophysical Research: Oceans*, 107(C8):10–1, 2002. B.2.1

A. Sheremet, S. Burke, and A. Maurer. Movement enhances the nonlinearity of hippocampal theta. *Journal of Neuroscience*, 36(15):4218–4230, 2016a. 2.2, 3.1.1, B.2, B.2

Alex Sheremet, Sara N Burke, and Andrew P Maurer. Movement enhances the nonlinearity of hippocampal theta. *Journal of Neuroscience*, 36(15):4218–4230, 2016b. 1, 3.1, 3.3.3

Alex Sheremet, Yuchen Zhou, Jack P Kennedy, Yu Qin, Sara N Burke, and Andrew P Maurer. Theta-gamma coupling: a nonlinear dynamical model. *bioRxiv*, page 304238, 2018. 1, 4

Evgenia Sitnikova, Alexander E Hramov, Alexey A Koronovsky, and Gilles van Luijtelaar. Sleep spindles and spike–wave discharges in EEG: their generic features, similarities and distinctions disclosed with Fourier transform and continuous wavelet analysis. *Journal of neuroscience methods*, 180(2):304–316, 2009. 4

OV Sosnovtseva, AN Pavlov, NA Brazhe, AR Brazhe, LA Erokhova, GV Maksimov, and Erik Mosekilde. Interference microscopy under double-wavelet analysis: a new approach to studying cell dynamics. *Physical review letters*, 94(21):218103, 2005. 4

G. Strang. *Linear Algebra and its Applications*. Harcourt-Brace & Comp., 1986. B.1.1

R.S. Strichartz. *A Guide to Distribution Theory and Fourier Transforms* . CRC Press Inc, 1994. B.1.1

Ch Stumpf. Drug action on the electrical activity of the hippocampus. In *International Review of Neurobiology*, volume 8, pages 77–138. Elsevier, 1965. 1, 4

David Sullivan, Jozsef Csicsvari, Kenji Mizuseki, Sean Montgomery, Kamran Diba, and György Buzsáki. Relationships between hippocampal sharp waves, ripples, and fast gamma oscillation: influence of dentate and entorhinal cortical activity. *Journal of Neuroscience*, 31(23):8605–8616, 2011. 2.2, 3.2

A. Swami, J.M. Mendel, and C.L. Nikias. *Higher Order Spectral Analysis Toolbox: A MATLAB toolbox for spectral and polyspectral analysis, and time-frequency distributions*. United Signals & Systems, 2001. A.3

Catherine Tallon-Baudry and Olivier Bertrand. Oscillatory gamma activity in humans and its role in object representation. *Trends in cognitive sciences*, 3(4):151–162, 1999. 4

Alejandro Terrazas, Michael Krause, Peter Lipa, Katalin M Gothard, Carol A Barnes, and Bruce L McNaughton. Self-motion and the hippocampal spatial metric. *Journal of Neuroscience*, 25(35): 8085–8096, 2005. 2.2

Adriano BL Tort, Robert W Komorowski, Joseph R Manns, Nancy J Kopell, and Howard Eichenbaum. Theta–gamma coupling increases during the learning of item–context associations. *Proceedings of the National Academy of Sciences*, 106(49):20942–20947, 2009. 1

Vladimir P Tychinskii. Coherent phase microscopy of intracellular processes. *Physics-Uspekhi*, 44(6):617, 2001. 4

C Ho Vanderwolf, R Kramis, LA Gillespie, and BH Bland. Hippocampal rhythmic slow activity and neocortical low-voltage fast activity: relations to behavior. In *The hippocampus*, pages 101–128. Springer, 1975. 1

Case H Vanderwolf. Hippocampal electrical activity and voluntary movement in the rat. *Electroencephalography and clinical neurophysiology*, 26(4):407–418, 1969. 1, 2.2

V.S. Vladimirov. *Methods in the theory of generalized functions*. Taylor & Francis, 2002. B.1.1

H. Weber. De Pulsa Resorptione Auditu et Tactu. *Annotationes Anatomicae et Physiologicae*, 1860. 2.2

P. D. Welch. The Use of Fast Fourier Transform for the Estimation of Power Spectra: A Method Based on Time Aver. aging Over Short, Modified Periodograms. *IEEE Transactions on Audio and Electroacoustics*, 15:70–73, 1967. B.3

IQ Whishaw and C Hippocampal Vanderwolf. Hippocampal EEG and behavior: change in amplitude and frequency of RSA (theta rhythm) associated with spontaneous and learned movement patterns in rats and cats. *Behavioral biology*, 8(4):461–484, 1973. 1, 3.1

Jean-Paul L Wiegand, Daniel T Gray, Lesley A Schimanski, Peter Lipa, CA Barnes, and Stephen L Cowen. Age is associated with reduced sharp-wave ripple frequency and altered patterns of neuronal variability. *Journal of Neuroscience*, 36(20):5650–5660, 2016. 2.2

Matthew A Wilson and Bruce L McNaughton. Reactivation of hippocampal ensemble memories during sleep. *Science*, 265(5172):676–679, 1994. 1

Jonathan Winson. Loss of hippocampal theta rhythm results in spatial memory deficit in the rat. *Science*, 201(4351):160–163, 1978. 2.1, 4

Chenguang Zheng, Kevin Wood Bieri, Sean Gregory Trettel, and Laura Lee Colgin. The relationship between gamma frequency and running speed differs for slow and fast gamma rhythms in freely behaving rats. *Hippocampus*, 25(8):924–938, 2015. 1, 3.1

Chenguang Zheng, Kevin Wood Bieri, Ernie Hwaun, and Laura Lee Colgin. Fast gamma rhythms in the hippocampus promote encoding of novel object-place pairings. *eNeuro*, pages ENEURO–0001, 2016. 1